Materials & Design 227 (2023) 111770

Contents lists available at ScienceDirect

Materials & Design

journal homepage: www.elsevier.com/locate/matdes

Unraveling the ultrahigh modulus of resilience of Core-Shell SU-8 nanocomposite nanopillars fabricated by vapor-phase infiltration

Zhongyuan Li [a,*], Jinlong He [b], Ashwanth Subramanian [c], Nikhil Tiwale [d], Keith J. Dusoe [e], Chang-Yong Nam [c,d], Ying Li [f,*], Seok-Woo Lee [a]

[a] Department of Materials Science and Engineering & Institute of Materials Science, University of Connecticut, 97 North Eagleville Road, Unit 3136, Storrs, CT 06269-3136, United States
[b] Department of Mechanical Engineering, University of Connecticut, 191 Auditorium Rd. U-3139, Storrs, CT 06269, United States
[c] Department of Materials Science and Chemical Engineering, Stony Brook University, Stony Brook, NY 11794, United States
[d] Center for Functional Nanomaterials, Brookhaven National Laboratory, Upton, NY 11973, United States
[e] University of Massachusetts at Amherst, Department of Polymer Science and Engineering, 120 Governors Drive, Amherst, MA 01003-9263, United States
[f] Department of Mechanical Engineering, University of Wisconsin-Madison, 1513 University Ave, Madison, WI 53706, United States

HIGHLIGHTS

- AlO_x/SU-8 nanocomposite nanopillars with core–shell structure were synthesized by Vapor-Phase Infiltration method.
- Core shell regions possess unique interconnecting-particulate microstructures that cannot be obtained by a conventional solution-based method.
- Polymer-like Young's modulus and metal-like high yield strength lead to a modulus of resilience close to its theoretical upper limit.
- Negligible strain-rate dependence of modulus of resilience attributes to the viscoelasticity of SU-8 with the low degree of cross-linking.
- Our work provides an optimized composite microstructural design that can absorb a large amount of elastic energy.

GRAPHICAL ABSTRACT

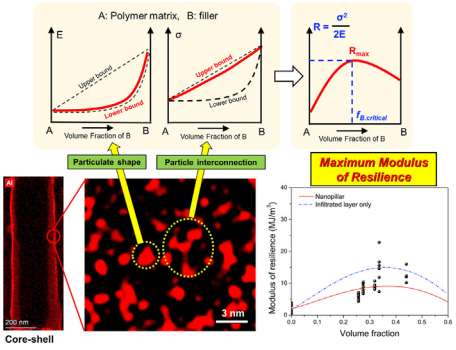

ARTICLE INFO

Article history:
Received 11 November 2022
Revised 16 January 2023
Accepted 16 February 2023
Available online 17 February 2023

Keywords:
Modulus of resilience
Elasticity
Nanocomposite
Vapor-phase infiltration

ABSTRACT

Modulus of resilience, the maximum strain energy density that can be stored in an elastically deformed solid, is an important mechanical property for developing artificial muscles in robotics, soft electronics panels, and micro-/nano-electromechanical actuators. In this study, core–shell SU-8 nanocomposites were fabricated via vapor-phase infiltration of nanoscale amorphous aluminum oxides into SU-8 nanopillars and performed transmission electron microscopy, nanomechanical testing, analytical modeling, and atomistic simulations to gain a fundamental insight into the ultrahigh modulus of resilience much higher than that of most high-strength materials. This study shows that the ultrahigh modulus of resilience results from: the low aspect ratio of amorphous aluminum oxide nano-particulates; the particulate size thicker than the free volume size; and the thin aluminum oxide interconnecting links within nano-particulates. These unique microstructural features produce the unusual combination of low specific

* Corresponding authors.
E-mail addresses: zhongyuan.li@uconn.edu (Z. Li), yli2562@wisc.edu (Y. Li).

https://doi.org/10.1016/j.matdes.2023.111770

SU-8 negative photoresist

Young's modulus (E), 4 MPa/(kg/m^3), and high specific yield strength (σ_y), 0.2 MPa/(kg/m^3), leading to the specific modulus of resilience, 5.21 ± 0.39 kJ/kg ($\sigma_y^2/(2E)$) about ten times higher than materials with the similar yield strength. This study demonstrates that vapor-phase infiltration is an excellent fabrication method to produce a polymer nanocomposite that can absorb and release a large amount of elastic strain energy.

1. Introduction

Modulus of resilience is the maximum strain energy density stored in an elastically deformed solid before plastic deformation occurs [1]. Achieving high modulus of resilience is desirable in various engineering applications. For instance, a material with a high modulus of resilience can absorb a large amount of mechanical work per given volume and can still be recovered to its original state. Thus, it can provide great protection from external mechanical work [2,3]. Also, artificial muscles in robots usually require a high modulus of resilience because artificial muscles that store a large amount of elastic energy can produce high-powered locomotion [4–6]. Advanced flexible electronics panels also require a high modulus of resilience because they require durability and flexibility simultaneously [7,8]. The modulus of resilience of isotropic linear elastic solids is defined as $\sigma_y^2/(2E)$, where σ_y is the yield strength and E is Young's modulus, and the simultaneous achievement of high σ_y (durability) and low E (flexibility) corresponds to high $\sigma_y^2/(2E)$. In addition, actuators in micro-/nano-electromechanical systems (MEMS/NEMS) often require a high modulus of resilience to achieve efficient energy conversion and high detection sensitivity [9–11].

However, it has been challenging to design a material with a high modulus of resilience. Because the yield strength and Young's modulus of most engineering materials usually scale together, $\sigma_y^2/(2E)$ does not increase significantly regardless of material class [12]. Nonetheless, it has been considered that a polymer composite would be a promising candidate material to achieve high modulus of resilience because a polymer matrix can serve as a starting material with a low Young's modulus. If a compositization process can improve the yield strength much more significantly than Young's modulus, it would be possible to achieve a high modulus of resilience. A composite model often shows that there are theoretical upper and lower bounds of Young's modulus [13] and yield strength [14] (Fig. 1(a) and (b)). Based on $\sigma_y^2/(2E)$, if Young's modulus of polymer composites is close to the theoretical lower bound (red line in Fig. 1(a)) but the yield strength is close to the theoretical upper bound (red line in Fig. 1(b)), the modulus of resilience can be maximized. Usually, the shape of the upper bound curve is close to that of the linear mixture rule, and the shape of the lower bound curve looks parabolic. If these two curves are inserted into $\sigma_y^2/(2E)$, the maximum modulus of resilience is expected to be achieved at a certain large volume fraction of filler ($f_{B,critical}$ in Fig. 1 **(c)**).

To obtain the high yield strength, it is usually better to have a small-sized filler because its high surface-to-volume ratio produces a large total interfacial area (per volume) where the interfacial interaction (or adhesion) makes plastic deformation more difficult [15,16]. Thus, a polymer nanocomposite, which contains nanoscale fillers, could be considered as a good candidate to achieve high modulus of resilience due to the combination of high matrix-filler interaction and low Young's modulus of the polymer matrix. However, it has been difficult to introduce a large volume of nano-sized filler, for instance, over 30 % of volume fraction into a polymer matrix ($f_{B,critical}$ in Fig. 1**(c)**), without filler agglomeration, which is detrimental to the mechanical properties of composites. In the case of conventional solution-based compositization methods, fillers almost always tend to agglomerate due to the high interfacial energy between filler and matrix. The agglomerated fillers usually degrade the mechanical properties of composites because it reduces the load bearing capacity of materials due to the weak binding at the filler-filler contact as well as the incomplete adhesion between filler agglomerates and matrix. Therefore, it is crucial to distribute nanoscale fillers uniformly into a matrix material without their agglomeration [17–19].

Recently, vapor-phase infiltration (VPI), also known as sequential infiltration synthesis (SIS), has been developed as a new compositization method to create polymer nanocomposites [20–22]. The molecular diffusion of vapor-phase precursors into the solid-state polymer network structure could distribute nanoscale metal oxides much more uniformly than conventional solution-based compositization methods. VPI techniques have been usually used to control the functionality of polymer surface for applications in microelectronics, energy storage, smart coatings, and smart fabrics [23]. However, the preliminary study confirmed that the VPI of amorphous aluminum oxide (a-AlO_x) nano-particulates into the SU-8 polymer matrix also produces polymer-nanocomposite nanopillars and demonstrated a strong potential as a structural material [24]. This work showed the possibility to fabricate nanocomposites with superior modulus of resilience, but the experimental data have been neither quantitatively understood by using analytical composite models nor understood from the perspective of nanoscale structures. Analytical composite models allow us to evaluate and predict the mechanical properties of nanocomposites in the wide range of the volume fraction of filler, even up to the range that an experiment cannot access. Meanwhile, atomistic simulation can probe the nanoscale origin of mechanical behavior. Therefore, it is worthwhile to use both analytical modeling and atomistic simulation to gain a fundamental insight into the processing-structure–property relation of the polymer nanocomposites. Furthermore, the internal nanostructure of nanopillars in the previous study was inferred from an infiltrated thin film. To relate the experimentally measured mechanical properties to the internal nanostructure, it is important to perform a detailed microstructural analysis, including compositional mapping directly on the infiltrated nanopillars.

In this study, therefore, we conducted extensive experimental and numerical studies on the internal nanostructural characteristics of a-AlO_x infiltrated SU-8 nanopillars to understand the fundamental origins of their exceptionally high modulus of resilience, orders of magnitude higher than most engineering materials. The high-resolution energy-dispersive X-ray spectroscopy (EDXS) images of nanopillar cross-section confirmed that the infiltrated nanopillar indeed has a core–shell structure where a-AlO_x nanoparticulates were overall evenly distributed in the SU-8 matrix, with some of them connected through ultrathin a-AlO_x links. The modified Halpin-Tsai (mHT) model [25], the modified Nicolais-Narkis (mNN) model[26], and the Hashin-Shtrikman (HS) model [13,14] revealed that the Young's modulus of the infiltrated layer is close to the HS lower bound while the yield strength of the infiltrated layer is close to the HS upper bound, leading to the ultrahigh

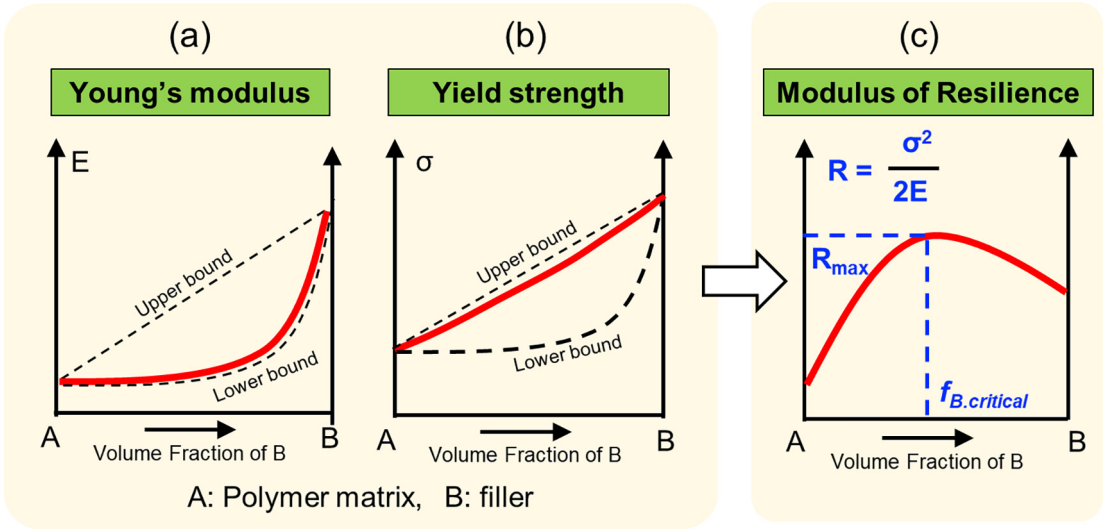

Fig. 1. Schematic diagram of (a) Young's modulus (E); (b) yield strength (σ_y); (c) modulus of resilience (R) of polymer composites as a function of volume fraction of reinforcement filler. The maximum possible modulus of resilience can be achieved at the critical volume fraction of filler, $f_{B,critical}$, which corresponds to a relatively large volume fraction.

modulus of resilience as described schematically in Fig. 1. In addition, molecular dynamics (MD) simulation results explain the critical roles of particle size and the degree of cross-linking (DC) of SU-8 matrix in the strain rate dependence of mechanical properties of nanocomposites. The quantitative analysis in this study provides an important insight into understanding the high modulus of resilience of polymer nanocomposites prepared by VPI. The results clearly show that the infiltration of nanoscale metal oxides into a polymer matrix via VPI is an excellent method for producing polymer nanocomposites with high modulus of resilience, which will be greatly beneficial for developing a reliable mechanical protector, high-powered artificial muscles in robotics, strong-but-flexible soft electronics panels, and ultrahigh-sensitive sensors in MEMS/NEMS applications.

2. Method

2.1. SU-8 nanopillar patterning and Vapor-Phase infiltration

The entire SU-8 nanopillar arrays patterning process was done by using a 100 kV JEOL JBX-6300FS electron-beam lithography system. SU-8 2002 (MicroChem) was diluted first and was spin-cast on the Si substrate under the speed of 2000–5000 rpm. Then, the sample was baked for 1 min at 65 ℃ (hot-plate baking) and was baked for another 1 min at 95 ℃ (soft baking). Electron-beam patterning with an exposure dose of 20 μC/cm^2 and 300 pA beam currents was followed, and the array of nanopillars was formed by cross-linking. The post-exposure SU-8 was baked for 1 min at 90℃ and then emerged in the propylene glycol monomethyl ether acetate (PGMEA) for 10 min to remove the SU-8 that were not cross-linked. Finally, the pattern of the SU-8 array was fully purged by isopropanol and dried by blowing N_2. The diameter and the height of the final SU-8 nanopillar are 300 nm and ~1 μm, respectively.

AlO_x-infiltrated core–shell SU-8 composite nanopillars were produced by the vapor-phase infiltration (VPI) method at 85 °C using the microdose protocol [27]. Using a conventional atomic layer deposition (ALD) system (Cambridge NanoTech, Savannah S100), the patterned SU-8 nanopillar arrays on a Si substrate were first exposed to vapor-phase organometallic Al precursor, trimethylaluminum (TMA, Sigma-Aldrich), by repeatedly dosing TMA vapor (14 msec pulsing duration) every 0.5 min for 20 times (thus, the total exposure time of 10 min (30 *sec* × 20)) under static vacuum (i.e., the chamber was isolated from a vacuum pump; pressure below 100 Torr), allowing TMA infiltration into the polymer matrix. This was followed by the nitrogen chamber purging (20 sccm) under dynamic vacuum for 10 min to remove unreacted TMA from the polymer matrix, completing the first half VPI cycle. Then, the TMA-infiltrated SU-8 nanopillars were similarly exposed to water vapor for 10 min via the microdose protocol (30 *sec* × 20; pulsing duration of 40 msec) under static vacuum (pressure ~ 20 Torr) followed by 10 min nitrogen purging to complete the first AlO_x VPI cycle, leading to the conversion of pre-infiltrated TMA to a-AlO_x. VPI with 4, 8, 12 cycles were done on the SU-8 nanopillars.

A quartz-crystal microgravimetry (QCM) system (Colnatec) was installed in the ALD chamber to measure the mass gain to calculate the volume fraction of a-AlO_x during the VPI process. Spin-cast more than 1 μm thick SU-8 film was done on the AT-cut quartz crystal (Philips Technologies, 6 MHz resonant frequency) which is Au-plated and has a diameter of 14 mm. The film was then soft baked and followed by exposure to ultraviolet (UV) light for 5 min in an N_2 environment (American Ultraviolet Co.) for cross-linking. After properly cross-linked, post-exposure baking was processed. The resonance frequency change was recorded during the VPI process and was transformed to mass gain results by the Sauerbrey equation. The sensitivity factor here is 81.2 Hz μg^{-1}cm^2.

2.2. Microstructural and mechanical characterizations

The microstructure details were studied by cross-sectional high-resolution transmission electron microscopy (TEM) (Talos™, 200 kV, ThermoFisher). TEM samples were prepared by focused ion beam (FIB) technique (FEI Helios) with a Pt protective layer deposited on the surface of the film. The high-angle annular dark field (HAADF) imaging and energy dispersive X-ray spectroscopy (EDXS) mapping were utilized to identify the distribution of infiltrated-AlO_x in SU-8 polymer nanopillars.

The mechanical properties of SU-8 polymer composite nanopillars were characterized by a NanoFlip™ (KLA, USA) which was installed in a field-emission scanning electron microscope (SEM) (JSM-6335F, JEOL, Japan). A diamond flat punch tip was used to

compress the nanopillars. The nanopillars were compressed at constant nominal displacement rates of 10, 100, and 1000 nm/s ($10^{-2}s^{-1}$, $10^{-1}s^{-1}$, and $1\ s^{-1}$), respectively and the corresponding stress–strain curves were obtained from the load–displacement data. Note that the strain rate dependence has not been studied before. The whole deformation process was recorded in-situ to confirm that no error was made in the mechanical measurement. Young's modulus was determined by using the linear fitting on stress–strain data at the initial stage of deformation. Because stress–strain curve is not perfectly linear, the strain value (ε_{ms}) that has the maximum slope ($d\sigma/d\varepsilon$) was determined first. Then, the linear fitting was done between $0.9\varepsilon_{\mathrm{ms}}$ and $1.1\varepsilon_{ms}$. Once Young's modulus is determined, the 1 % offset of plastic strain was used to determine yield strength.

2.3. Fullerene-reinforced SU-8 polymer atomic model

Here, fullerene was used instead of a-AlO_x particulate to reduce the computational cost. If a-AlO_x particulate is used, MD simulation will need to compute the position and velocity of all Al and O atoms, most of which do not interact with SU-8 molecules. Fullerene has a much smaller number of atoms, but its high stiffness and weak interaction with SU-8 molecules can mimic the role of a-AlO_x particulate in the nanocomposite.

A cross-linked and fullerene-reinforced SU-8 polymer model was computationally generated on account of a multi-step cross-linking scheme. Taking 50 % DC SU-8 polymer filled with the volume fraction of 5 % C20 fullerene particles as an example, reactive atoms are first assigned to two SU-8 monomers (SU-8–1 and SU-8–2). Here, the end carbon atoms, and oxygen atoms of the epoxide groups are set to the reactive atoms of SU-8–1 and SU-8–2 monomers, respectively. Then employing a $10 \times 10 \times 10\ nm^3$ cubic box along x, y, and z-direction, 205 SU-8–1 monomers, 205 SU-8–2 monomers, and 289 C20 particles are packed into a 3D-periodic amorphous cell in which SU-8 monomers and C20 particles can move randomly in a box, and there are 1640 potential reaction sites in the total system (eight sites for each SU-8 monomer).

Next, geometry optimization and 5 annealing cycles are performed for equilibrating the packed system with periodic boundary conditions in all directions. During the whole equilibration process, constant pressure and constant temperature are controlled by the Andersen barostat and the Nose–Hoover thermostat, respectively. After the equilibration process, the SU-8 model is polymerized by applying a cross-linking criterion to achieve a target DC and remove the possible geometric distortions. As the cross-linking reactions are usually performed for the SU-8 model at an ascended temperature, a similar equilibration process is applied to relax the structure at the risen temperature before conducting cross-linking reactions. The temperature is set up at 368 K to match the temperature of the fabrication process of SU-8 samples. At each cross-linking step, the distance between the available reactive atoms is first calculated, and then possible reactive atoms situated in the current cutoff are identified. The initial cutoff distance is set to be 4.5 Å with an increment of 0.5 Å, and the maximum cutoff distance is set to be 14.0 Å. When the reactive atoms are determined, the epoxide groups consisting of those discerned reactive atoms are open. Virtual elastic springs are developed between those reactive atoms within the opened epoxide groups at a given cutoff distance. Those discerned reactive atoms are then pulled together under the virtual elastic springs to develop cross-links when the distance between those reactive atoms is short enough (less than 0.147 nm). After the cross-links are formed, the unreacted atoms are compensated with hydrogen atoms for the open epoxide groups. After each cross-linking step, the geometric configuration is updated by adding new bonds, angles, dihedral angles, and improper angles into the cross-linked structure. Geometry optimization and 5 annealing cycles are further performed for the new geometric configuration to alleviate geometric distortions. After that, the next cross-linking step continues to be carried out until the DC reaches 50 %. When the DC is satisfied, the cross-linking simulation stops further epoxide groups breaking and bond formation, eventually building up a fullerene-reinforced SU-8 polymer. Besides, a short equilibrium process is conducted to cool down the developed cross-linked structure until room temperature is achieved. During the cross-linking process, partial charges are also updated to obey the charge neutrality and force field assignment. Finally, structure optimization and 40 annealing cycles are performed for the built SU-8 polymer.

2.4. Model systems for MD simulations

The focused SU-8 polymer systems in this study include pure SU-8 polymers with different DCs and fullerene-reinforced SU-8 polymers with different filler sizes and volume fractions. Six different DCs are considered for pure SU-8 polymers, such as 20 %, 30 %, 40 %, 50 %, 60 %, and 70 %. For fullerene-reinforced SU-8 polymer, 50 % DC is employed for all simulation systems. Then, nine size fillers are studied, such as C20, C36, C60, C84, C180, C240, C320, C540, and C720, corresponding to a radius of 0.346 nm, 0.417 nm, 0.494 nm, 0.551 nm, 0.707 nm, 0.777 nm, 0.855 nm, 1.018 nm, and 1.121 nm, respectively. Additionally, the initial and final volume fractions for different filler types are listed in **Table S4**. Here, the final volume fraction of filler is determined based on the equilibrium configuration of MD simulations.

2.5. MD simulations process for mechanical metrics

All MD simulations are conducted using the Large-scale Atomic/Molecular Massively Parallel Simulator (LAMMPS) package [28]. Interaction potentials involving fullerene particles and SU-8 polymer are characterized by polymer consistent force field (PCFF) [29–31]. PCFF is a verified second-generation force field, which has been parameterized for organic compounds and widely applied to describe materials' mechanical properties, compressibility, elastic constants, and so on. Non-bonded interactions, including LJ and Coulomb potentials, are defined as:

$$U_{\mathrm{nonbonded}} = \varepsilon_{ij}\left[2\left(\frac{\sigma_{ij}}{r_{ij}}\right)^{9} - 3\left(\frac{\sigma_{ij}}{r_{ij}}\right)^{6}\right] + C\frac{q_i q_j}{\varepsilon r_{ij}} \tag{12}$$

where r_{ij} is the distance between atoms i and j, ε_{ij} denotes the depth of the LJ potential well between two atoms, q_i and q_j denote the charges of atoms i and j, respectively. σ_{ij} represents the interatomic distance at which the LJ potential gives the minimum value. C defined as a unit conversion factor and ε is a dielectric constant. The interaction potentials between different types of atoms are calculated using the six-power mixing rules[32]: $\varepsilon_{ij} = \sqrt{\varepsilon_i \varepsilon_j}\, 2 r_{ii}^3 r_{jj}^3 \left(r_{ii}^6 + r_{jj}^6\right)^{\frac{1}{2}}$ and $\sigma_{ij} = 2^{\frac{1}{6}}\left(\sigma_{ii}^6 + \sigma_{jj}^6\right)^{\frac{1}{6}}$. Electrostatic and Van der Waals interactions are truncated smoothly with a cutoff of 10.0 Å. Particle–particle particle–mesh (PPPM) solver with a force tolerance of 10^{-4} is used to calculate the long-range electrostatic interactions.

Before performing mechanical properties, simulation systems are equilibrated first using a 21-step MD equilibration protocol [33]. Based on the obtained equilibrium configuration, a relaxation time of 500 ps continues to be performed under the NPT ensemble at 300 K and 0.0 MPa. Using the NEMD simulation after equilibration, an improved stress–strain loading process [34] is employed to compress the system along the z-direction at 300 K with a time step of 0.2 fs. The z-dimension within the simulation box was

diminished during each loading stage in a $N\sigma_{ij}\varepsilon_{ij}T$ ensemble until an approximate engineering compressive strain of 30 % was achieved. Meanwhile, the system keeps at 0 MPa along both $\times$ and y directions during the loading process, allowing their dimensions to free change to meet the Poisson's effect. Two stain rates are employed for pure SU-8 polymers and fullerene-reinforced SU-8 polymer systems, including 10^8 s^{-1}, and 5×10^8 s^{-1}. Their mechanical metrics, elastic modulus (E), and yield strength (σ_y) are then extracted based on the obtained stress–strain curves.

3. Results

3.1. Microstructure of SU-8 nanocomposites

Core-shell SU-8 nanopillars were produced via VPI (Fig. 2) (**See also Method Section**). The TEM specimen in this study was fabricated directly from an infiltrated SU-8 nanopillar that underwent 12 VPI cycles. Cross-sectional energy dispersive X-ray spectroscopy (EDXS) mapping was performed for different elements (Fig. 3). Signals for Al element confirm ~50 nm infiltration depth from the side surface of the nanopillar (Fig. 3**(a)**). Therefore, the TEM results confirm that the nanocomposites have a core–shell structure that consists of a pure SU-8 core with ~200 nm in diameter and a ~50 nm-thick infiltrated shell. Al and additional O exhibit nearly identical shape of concentration profile within the infiltrated region (Fig. 3**(b)-3(d)**), which also supports the formation of AlO_x via VPI inside the SU-8 matrix.

Note that the SU-8 matrix is expected to have a significantly large free volume compared to other polymers due to the cage-like open structure of the SU-8 monomer (~1 nm size curved shape, **the inset of** Fig. 2**(a)**). Because it is difficult to characterize free volume dimensions experimentally, MD simulation was performed to investigate the free volume structure by controlling the degree of cross-linking and minimizing the total energy of the system (**See also Method Section**). The results showed that the SU-8 matrix contains plenty of free volume channels ~0.4 nm in width and a few nm in length regardless of the degree of cross-linking (**See also Supplementary Information**). The free volume channel of the SU-8 matrix would allow the diffusion of TMA and water molecules into the SU-8 matrix. The high-resolution TEM image and its Fast Fourier Transform pattern confirm that there is no crystallinity (**See also Supplementary Information**), implying that AlO_x appears to be amorphous (a-AlO_x).

The high-resolution nanoscale EDXS mapping images show more details of the microstructure, which shows a homogenous and dense distribution of AlO_x nano-particulates in the polymer matrix (Fig. 4**(a) and 4(b)**), corroborating that VPI successfully created a uniform and dense distribution of a-AlO_x nano-particulates with almost no agglomeration. Interestingly, many clusters are interconnected by the ultrathin a-AlO_x structure (indicated by the green arrows in Fig. 4**(c)**). The observed AlO_x interconnects between

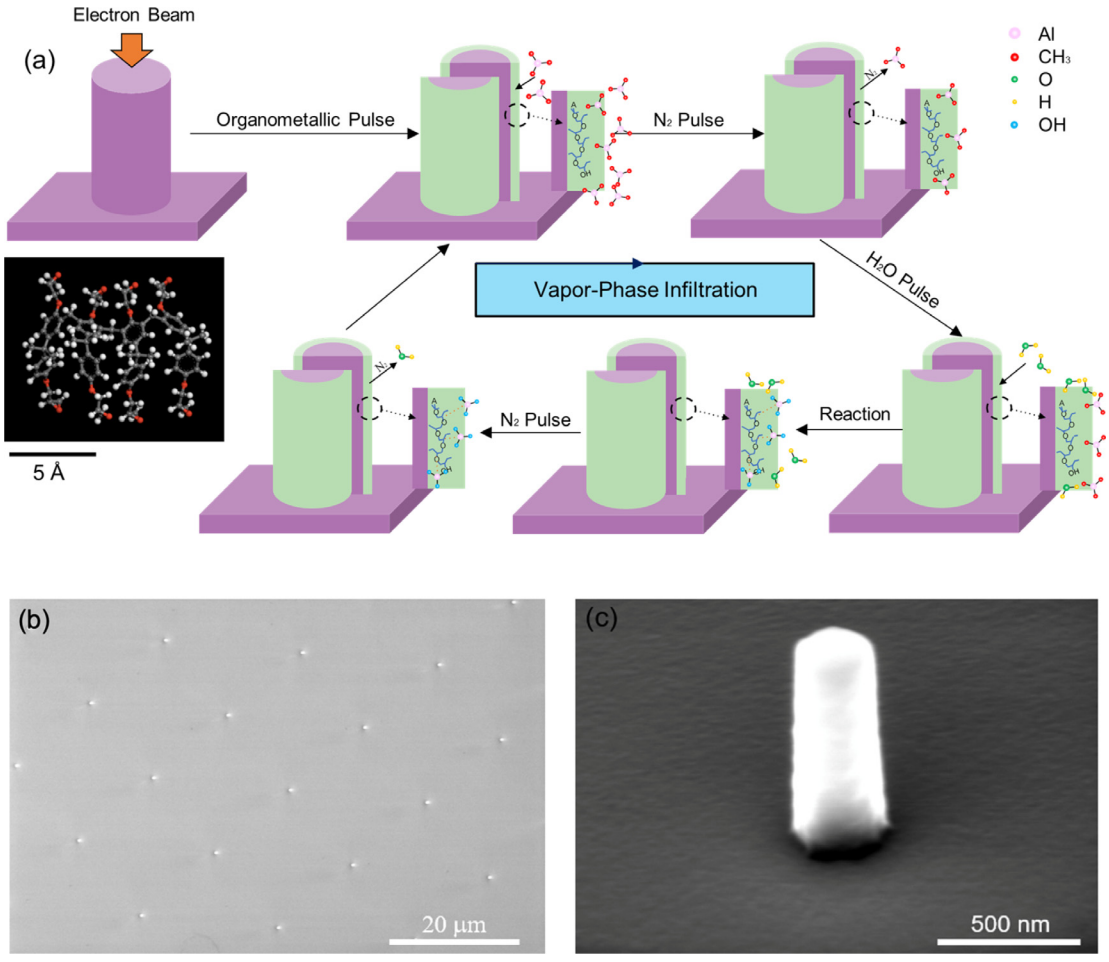

Fig. 2. (a) Schematic illustration of the preparation of a-AlO_x-infiltrated SU-8 nanopillar by combining electron-beam lithography and vapor-phase infiltration (VPI). Inset shows the structure of SU-8 monomer, which has the cage-like open structure with ~1 nm in width (b) SEM images of a-AlO_x-infiltrated SU-8 nanocomposite nanopillar array; (c) high magnification image of nanocomposite nanopillar.

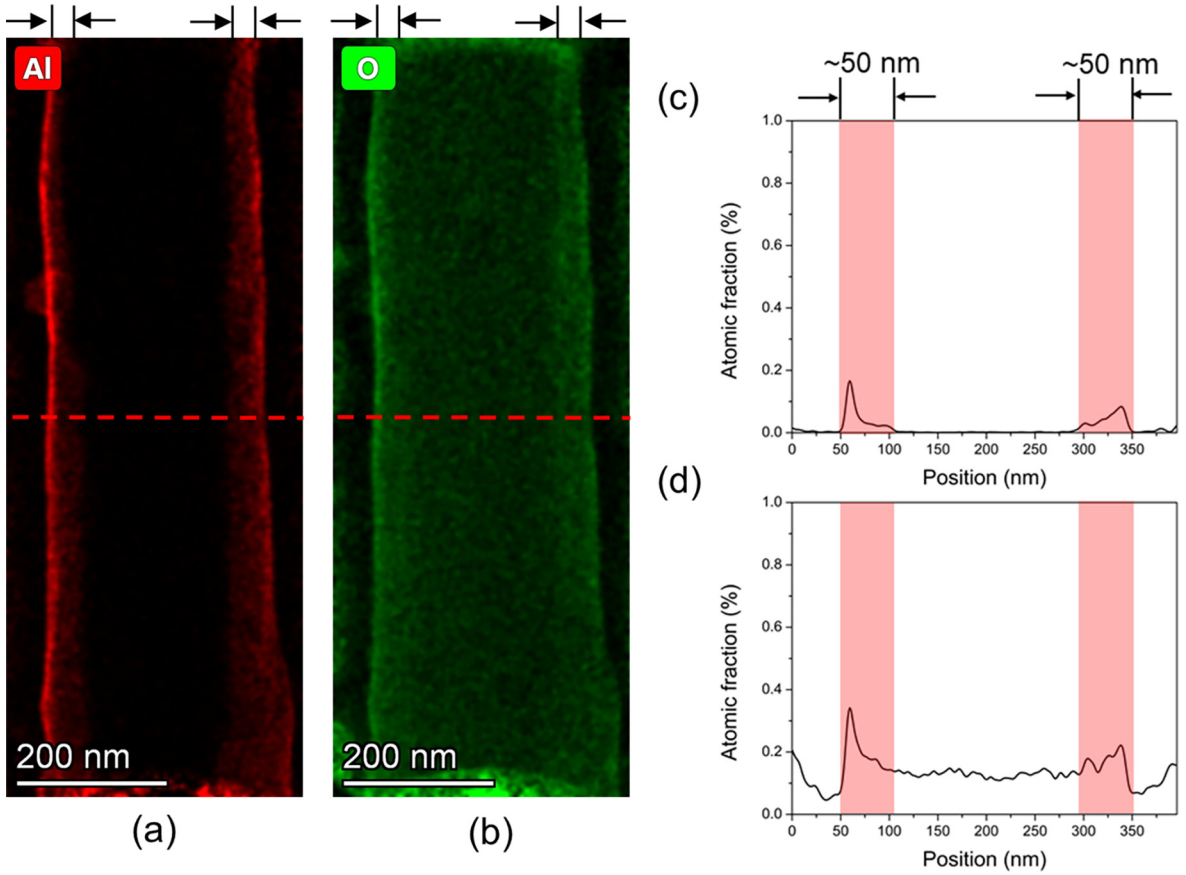

Fig. 3. Cross-sectional EDXS composition map of nanopillar with 12 infiltration cycles for (a) Al (b) O elements, and the corresponding composition profile of (c) Al and (d) O elements (scanned along the red dash lines). The infiltration depth is ~ 50 nm. (For interpretation of the references to colour in this figure legend, the reader is referred to the web version of this article.)

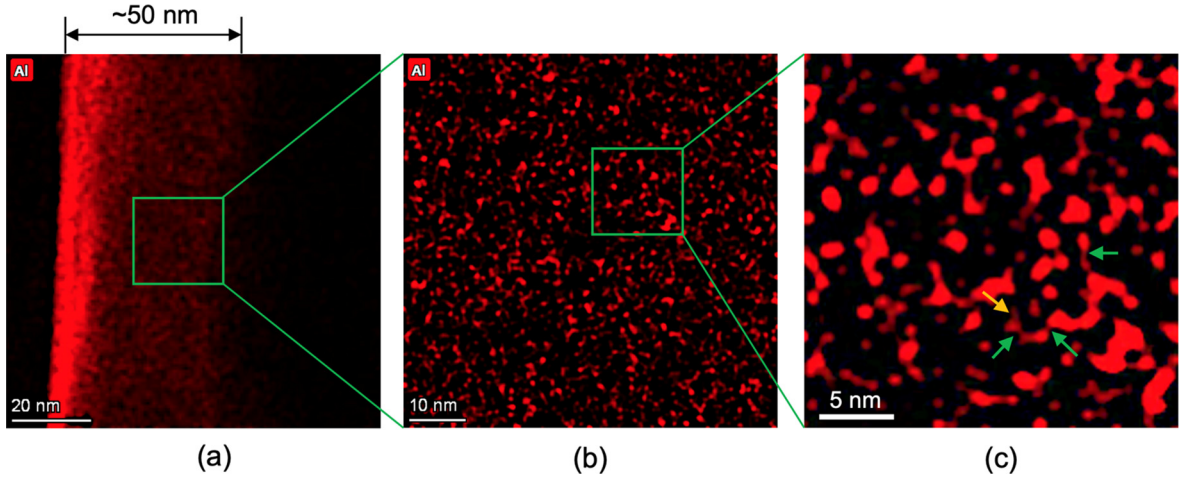

Fig. 4. High resolution EDXS mapping images of Al element in the infiltrated layer. (a) the lowest, (b) intermediate, and (c) the highest magnification. The green arrows indicate the interconnection between nano-particulates, and the orange arrow indicates the nanoscale hair emanating from nano-particulates. These unique features can be found in many other nano-particulates. (For interpretation of the references to colour in this figure legend, the reader is referred to the web version of this article.)

clusters most likely have been formed through channels among free volumes due to the open network structure of the SU-8 matrix. Previously, it has been shown that the metal oxide VPI, specifically ZnO, in SU-8 was mediated via residual solvent molecules (blue region in Fig. 5) with reactive moieties (such as C=O bond) that could interact with infiltrating Zn precursor, diethylzinc (DEZ). [20] Since both TMA and DEZ are Lewis acids, the reaction mechanism of TMA with SU-8 is expected to be similar to that of DEZ with SU-8. The formation of a-AlO_x in the SU-8 matrix during VPI should start on this basis, and the network should continue to grow through the channels among the neighboring free volume sites (Fig. 5), leading to interconnected nano-particulates.

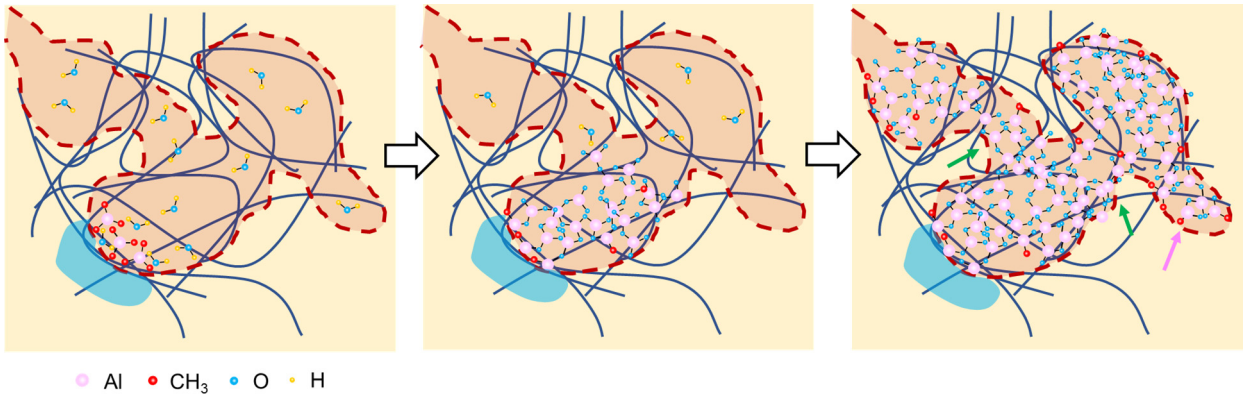

Fig. 5. Schematic diagram of the formation process of nano-particulates and its interconnection. The region surrounded by the red broken line indicates the free volume. The blue region corresponds to un-cross-linked SU-8 region with the residual solvent molecules. This region serves as a nucleation cite of nano-particulates. [20] The green arrows indicate interlink between nano-particulates, and the magenta arrows indicate the terminated links. (For interpretation of the references to colour in this figure legend, the reader is referred to the web version of this article.)

3.2. Micromechanical data

The representative engineering stress–strain curves were obtained from pure SU-8 nanopillars and AlO_x-infiltrated core–shell nanopillars with 4, 8 and 12 VPI cycles and at different strain rates (Fig. 6) (**See also Supplementary Information**). Increasing cycles of VPI increases both yield strength and Young's modulus simultaneously. To study the effects of infiltration quantitatively, the volume fraction of AlO_x filler needs to be measured. Since the in-situ quartz-crystal microgravimetry (QCM) system measures the amount of mass gain during VPI cycles (**See also Supplementary Information**), the volume fraction (f) of a-AlO_x filler in the infiltrated layer could be determined by the following equation:

$$f = \frac{M_{AlO_x}}{\rho_{AlOx} \cdot V_{infil}} \quad (1)$$

where M_{AlO_x} is the mass gain of a-AlO_x recorded by the in-situ QCM, ρ_{AlO_x} is the density of amorphous AlO_x filler (~3000 kg/m^3) and V_{infil} is the volume of the infiltrated layer. Note that only for the mass gain measurement, the SU-8 thin film sample had to be used because a nanopillar array is too small to absorb the measurable total mass of a-AlO_x. The calculation shows that the volume fraction of a-AlO_x in the infiltrated layer reaches up to 32 % for 12 infiltration cycles and 44 % for the 16 infiltration cycles in the previous study. [24] Both values are surprisingly high, compared to the typical value of polymer nanocomposites (less than 10 %[35–38]), most of which also show the significant agglomeration of fillers. Thus, the VPI can introduce an exceptionally large volume fraction of nanoscale oxide fillers uniformly into the infiltrated layer with almost no agglomeration.

Young's modulus (Fig. 7**(a)-(c)**) and yield strength (Fig. 7**(d)-(f)**) were obtained as a function of a-AlO_x volume fraction in the infiltrated layer and strain rate, respectively. Here, the yield strength was obtained based on 1 % offset yield strength. The large error in Young's modulus could result from the error in displacement rate caused by the PID-feedback loop, but the random nature of this error does not affect the average value much. Both Young's modulus and yield strength increase with the volume fraction of filler. For the high infiltration cycles, for instance, 12 cycles, the core–shell nanocomposites exhibit metal-like high strength (371.13 ± 10.58 MPa) but foam-like low Young's modulus (7.66 ± 0.35 GPa). Both Young's modulus and yield strength increases with strain rate, but the modulus of resilience is relatively insensitive to the strain rate (Fig. 7**(g)-(i)**).

3.3. Interphase models for the evaluation of mechanical performance

A theoretical model for analysis could provide a useful pathway to describe the relationship between the infiltrated layer's Young's modulus as well as its yield strength and the filler volume fraction, so as to achieve the modulus of resilience estimation for any specific filler volume fraction. Based on the presence of a-AlO_x nanoparticulates, the particulate composite model could be the best approximation that describes the mechanical properties of the infiltrated layer. Then, the mechanical properties of core–shell nanopillars can be estimated by using the isostrain model because

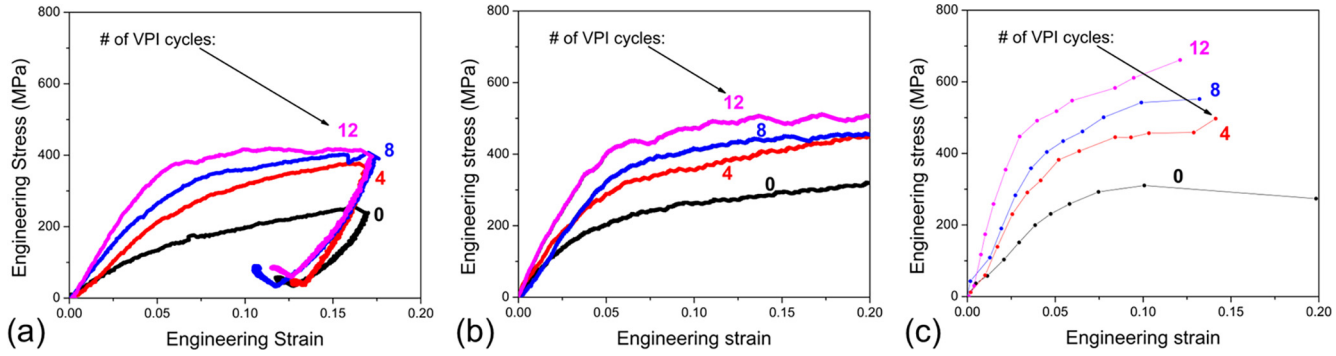

Fig. 6. Representative engineering stress–strain curves tested under the nominal strain rate of (a) 10^{-2} s^{-1} (b) 10^{-1} s^{-1}, and (c) 1 s^{-1}. The numbers (0, 4, 8, and 12) correspond to the number of infiltration cycle.

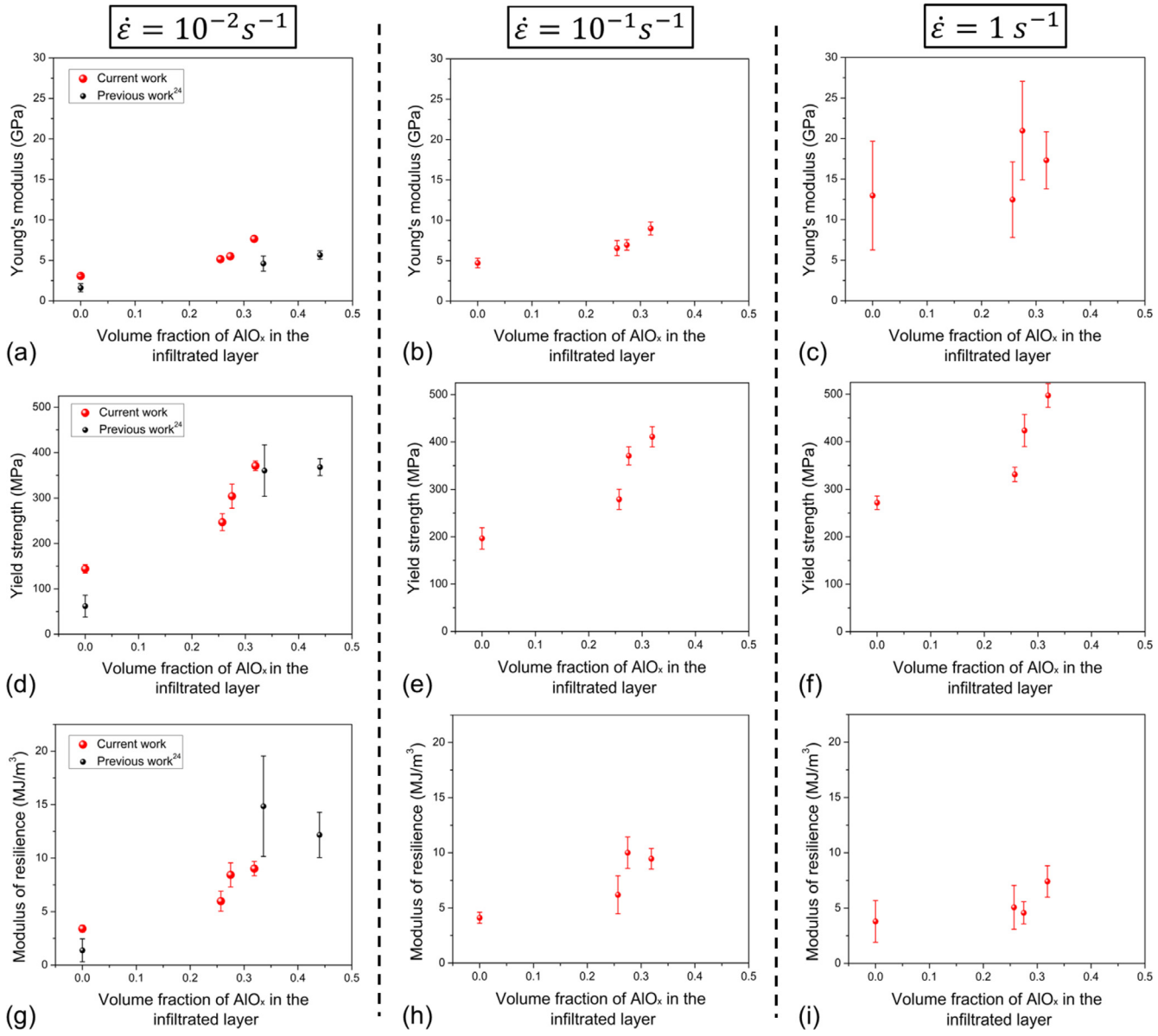

Fig. 7. Mechanical data as a function of volume fraction. Young's modulus under the strain rate of (a) 10^{-2} s^{-1} (b) 10^{-1} s^{-1}, and (c) 1 s^{-1}. Yield strength under the strain rate of (d) 10^{-2} s^{-1} (e) 10^{-1} s^{-1}, and (f) 1 s^{-1}. Modulus of resilience under the strain rate of (g) 10^{-2} s^{-1} (h) 10^{-1} s^{-1}, and (i) 1 s^{-1}. Note that we use the volume fraction of a-AlO_x in the infiltrated layer as the x-axis value instead of the volume fraction of a-AlO_x in the entire volume of pillar to be consistent with the other figures that contain mechanical properties of both composites and infiltrated layer as a function of the volume fraction of a-AlO_x in the infiltrated layer.

the loading direction is parallel to the infiltrated layer on the side surface.

Zare modified the original Halpin-Tsai (mHT) model [39] by materializing the interfacial interaction effect by introducing a hypothetical phase between nanoparticle and matrix, and this phase is termed as 'interphase' [25]. In this model, interphase parameters are just the fitting parameters that combine all additional contributions to mechanical properties, such as adhesion between filler and matrix, local matrix distortion, and chemical/structural mixing between filler and matrix. The structural mixing between filler and matrix could be particularly important because some a-AlO_x nano-particulates possess the interconnecting links (or its terminated form) between nano-particulates. Thus, we assume that a AlO_x nano-particulate consists of nanoparticle and interphase which is the structural mixture of SU-8 matrix and AlO_x nanoscale link.

The mHT model expresses Young's modulus of composite (E_C) with the following relation:

$$\frac{E_C}{E_M} = \frac{1 + 2\eta_p f + 2\eta_i f_i}{1 - \eta_p f - \eta_i f_i} \tag{2}$$

where $\eta_p = \frac{\frac{E_P}{E_M} - 1}{\frac{E_P}{E_M} + \zeta}$ and $\eta_i = \frac{\frac{E_i}{E_M} - 1}{\frac{E_i}{E_M} + \zeta}$. E_M and E_P in the Eq. (2) are the Young's modulus of the matrix and fillers, respectively. E_i and f_i are Young's modulus and volume fraction of interphase, respectively, and f_i is calculated by $\left[\left(\frac{R+t}{R}\right)^3 - 1\right]f$, where R is the radius of the filler, t is the thickness of the interphase and f is the volume fraction of nanoparticles. ζ is two times the aspect ratio of filler and is 2 for a spherical particle, which is approximately the case of this study. This mHT model (Eq. (2)) can provide the analytical expres-

sion of Young's modulus of the infiltrated layer as a function of volume fraction of a-AlO_x filler (such as Fig. 1**(a)**).

Furthermore, the yield strength of particulate composites can be predicted by the modified Nicolais-Narkis (mNN) model, which also includes the same interphase concept[26], which incorporates all additional strengthening components into the interphase strength (σ_i). The mNN model utilizes interfacial parameter 'a', which is a function of σ_i, to describe the degree of interfacial interaction between fillers and matrix, and the equation is expressed as:

$$\sigma_c = \sigma_m\left(1 - af^{\frac{2}{3}}\right) \tag{3}$$

where σ_c and σ_m are the yield strength of the composite and matrix, respectively. The effective interaction helps transfer a portion of the load from the matrix to fillers so that strengthens the whole material. In this case, the value of 'a' becomes the negative number, and σ_c increases. If the interphase is available, 'a' can be calculated as:

$$a = 1.21\left[\frac{(R+t)^2}{R^2} - \frac{\sigma_i}{\sigma_m}\left(\frac{(R+t)^2}{R^2}\right)\right] \tag{4}$$

where σ_i is the yield strength of interphase. Note that R and t must be the same in both the mHT model and mNN model.

In the mHT and the mNN model, the three unknown parameters are the mechanical properties of interphase (E_i and σ_i) and the thickness of interphase (t). These parameters can be obtained by fitting Eqs. (2) and (3) into the experimental data. Because these two models describe the mechanical properties of the infiltrated layer only and do not include the contribution of the SU-8 core. Thus, this isostrain core–shell model was used to fit into the experimental data of core–shell nanopillars. Due to the relatively weak chemical interaction between a-AlO_x nano-particulate and SU-8 matrix (chemical bonding occurs only at the residual solvent regions, the blue region in Fig. 5), the interphase thickness may not be larger than the radius of a-AlO_x particulate. Then, the different ratio of t/R between 0 and 1 was assumed with 1/10 of resolution. Also, if a filler grows as VPI cycles increase, the filler-matrix interaction will increase. Thus, the power law form of $E_i = C_1 V_f{}^m GPa$ and $\sigma_i = C_2 V_f{}^n MPa$ was used as the first order of approximation of the monotonic increase in E_i and σ_i. Here, the exponents, m and n, describe how sensitive Young's modulus and yield strength are to the volume fraction of filler, respectively. With this model set up, the numerical calculation discovered that $\frac{t}{R} = \frac{1}{3}$ gives approximately the best fitting with $E_i = \left(7.466 V_f{}^{0.1218}\right) GPa$ and $\sigma_i = \left(693.7 V_f{}^{0.2718}\right) MPa$.

With the obtained fitting parameters, it is now possible to estimate Young's modulus (Fig. 8**(a)**) and yield strength (Fig. 8**(b)**), and the modulus of resilience (Fig. 8**(c)**) of the infiltrated layer (blue dash line) and the core–shell composite (red line) as a function of volume fraction of filler in the infiltrated layer. Both curves show that the maximum modulus of resilience is obtained at around 36 % of the volume fraction of filler, which is close to the volume fraction of the highest experimental value (Fig. 8**(c)**). This result confirms theoretically that the infiltrated layer of the sample already reached the maximum possible modulus of resilience under the used synthesis conditions. Interestingly, a further increase in the volume fraction of filler decreases the modulus of resilience. This is primarily because Young's modulus increases much more rapidly than the yield strength at a higher volume fraction of filler (Fig. 8**(a) and 8(b)**). This result is exactly consistent with the hypothesis (Fig. 1). Therefore, the optimum volume fraction of filler is present for the highest modulus of resilience of a given composite system.

Note that a polymer nanocomposite has a much lower density compared to metals or ceramics. Thus, it is worthwhile to compare the modulus of resilience per mass density, which is called the specific modulus of resilience. The excellent specific modulus of resilience of the core–shell nanopillars can be highlighted when the data are plotted in the modified Ashby Chart of specific strength vs specific modulus (Fig. 9). The modified Ashby Chart shows that the core–shell nanopillars of this study exhibit an ultrahigh specific modulus of resilience (5.21 ± 0.39 kJ/kg) and occupy the white space, implying that it exhibits a unique combination of high specific strength and low specific modulus. It is also possible to extract the specific modulus of resilience of the infiltrated layer (6.28 ± 0.58 kJ/kg) by using the isostrain model. It was found that the specific modulus of resilience of the infiltrated layer is almost the same as that of the core–shell nanocomposite. For the fully infiltrated nanocomposite, the increase in mass density compensates the increase in modulus of resilience, which allows a core–shell nanocomposite to have a similar specific modulus of resilience to the fully infiltrated layer. This result implies that full infiltration is not always necessary for achieving the high modulus of resilience.

3.4. Upper and lower bounds of Young's modulus and yield strength

In the previous section, the mechanical performance of core–shell nanocomposite was evaluated by comparing the fitted data and the experimental data. The mHT and mMN models allowed us to find the maximum modulus of resilience, but this evaluation is valid only under the given synthesis condition. It is also worthwhile to compare the data with their theoretical values, which can be achieved in the idealized composite structure. The Hashin-

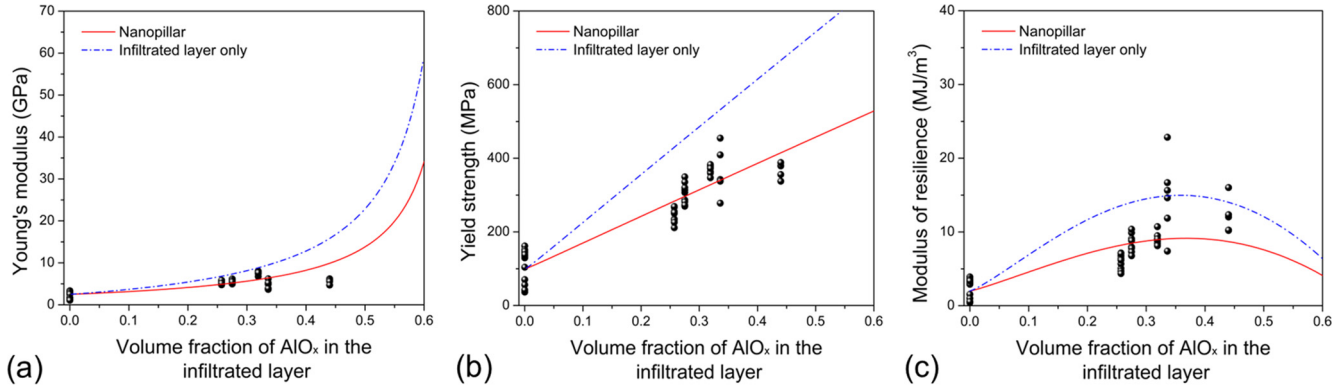

Fig. 8. (a) Experimental and calculated Young's moduli (the mHT model) as a function of volume fraction of AlO_x in the infiltrated layer; (b) Experimental and calculated yield strength (the mNN model) as a function of volume fraction of AlO_x in the infiltrated layer (c) Experimental and calculated modulus of resilience (the mNN model) as a function of volume fraction of AlO_x in the infiltrated layer. The fitted properties of composite nanopillar are represented by red line and the fitted properties of infiltrated layer are represented by blue dash line. (For interpretation of the references to colour in this figure legend, the reader is referred to the web version of this article.)

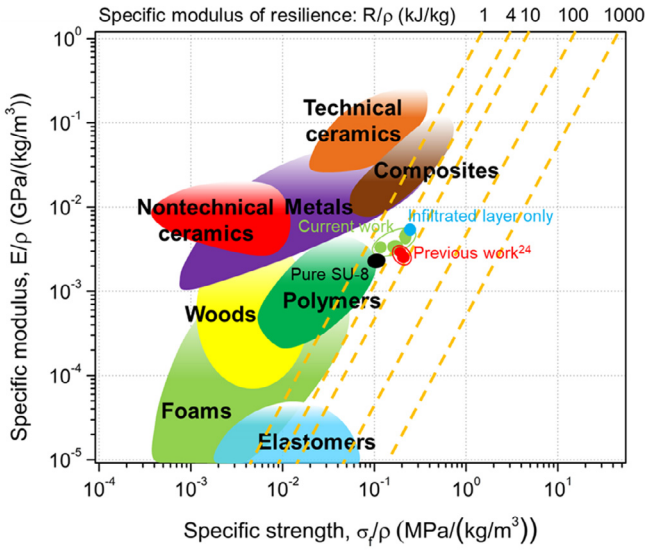

Fig. 9. A chart of specific strength vs specific modulus summarizing the mechanical properties of pure SU-8 nanopillars and AlO_x-infiltrated SU-8 nanopillars in comparison with other engineering materials. A broken line indicates the contour line with a given modulus of resilience.

Shtrikman (HS) model[13,14] is based on the variational principle of elasticity theory for linear and isotropic materials and has been extensively used to obtain the theoretical upper and lower bounds of Young's modulus and yield strength of composites with no interfacial interaction. The HS model predicts the lower bounds of bulk modulus 'K_L' and shear modulus 'G_L' as:

$$K_L = K_M + \frac{f}{\frac{1}{K_P - K_M} + \frac{3(1-f)}{3K_M + 4G_M}} \tag{5}$$

$$G_L = G_M + \frac{f}{\frac{1}{G_P - G_M} + \frac{6(1-f)(K_M + 2G_M)}{5G_M(3K_M + 4G_M)}} \tag{6}$$

and the upper bounds of bulk modulus 'K_H' and shear modulus 'G_H' as:

$$K_H = K_P + \frac{(1-f)}{\frac{1}{K_M - K_P} + \frac{3f}{3K_P + 4G_P}} \tag{7}$$

$$G_H = G_P + \frac{f}{\frac{1}{G_M - G_P} + \frac{6f(K_P + 2G_P)}{5G_P(3K_P + 4G_P)}} \tag{8}$$

where f is the volume fraction of fillers. K_M and G_M are the bulk and shear moduli of matrix, respectively, and K_P and G_P are the bulk and shear moduli of reinforcing particles, respectively. K and G can be calculated by the relation of E and Poisson's ratio v: $K = \frac{E}{3(1-2v)}$ and $G = \frac{E}{2(1+v)}$, where Young's modulus (E_M) of the matrix is set as 2 GPa, which is in agreement with the experimental result obtained from the stress–strain data (Fig. 7**(a)**). And the Young's modulus (E_P) and Poisson's ratio (v_P) of fillers and Poisson's ratio (v_M) of matrix are used as 173 GPa, [40] 0.24[41] and 0.26, [42] respectively. Then, the lower and upper bounds of E were calculated by $E_L = \frac{9K_L G_L}{3K_L + G_L}$ and $E_H = \frac{9K_H G_H}{3K_H + G_H}$, respectively.

The HS model also provides analogous upper (σ_H) and lower (σ_L) bounds for yield strength:

$$\sigma_H = \frac{5(1-f)\sigma_M}{3 + 2(1-f)} + \frac{3f\sigma_P}{3 + 2(1-f)}\sqrt{1 + \frac{2(1-f)}{3}\left[1 - \left(\frac{\sigma_M}{\sigma_P}\right)^2\right]} \tag{9}$$

and the lower bound of yield strength as:

$$\sigma_L = \sigma_M\sqrt{1 + 1.5f} \tag{10}$$

where σ_P is the yield strength of the strong phase and σ_M is the yield strength of the weak phase. The final upper bound of the modulus of resilience is obtained by using the upper bound of yield strength and the lower bound of Young's modulus as suggested in Fig. 1. All curves are plotted with the corresponding experimental data points (Fig. 10). Results show that the experimental Young's modulus is slightly higher than the lower bound but much lower than the upper bound (Fig. 10**(a)**). The experimental yield strength is almost the same as the upper bound (Fig. 10**(b)**). These results show that the nanocomposites indeed have the unusual combination of low Young's modulus and high yield strength, which is extremely difficult to achieve in most material systems. This should be the reason why the experimental modulus of resilience of nanocomposites occupies the white space in the modified Ashby Chart (Fig. 9).

4. Discussion

4.1. Low Young's modulus of nanocomposites

The equation of the mHT model (**Eq. (2)**) shows that Young's modulus of a particulate-filled composite is mainly the function of the aspect ratio and the volume fraction of filler. Thus, the effect of the aspect ratio of filler on Young's modulus of the nanocomposites was examined (Fig. 11**(a)**). The mHT model shows that as the aspect ratio increases, Young's modulus increases significantly. Also, it is worthwhile to note that for the volume fraction between 0 % and 44 % (the experimental range), Young's modulus with the aspect ratio of unity (the composite of this study, the black broken line in Fig. 11**(a)**) is close to the lower bound of the HS model, which corresponds to the theoretical minimum of Young's modulus of the composite. Therefore, the dominant factor that enabled the low Young's modulus of the nanocomposite is the low aspect ratio of a-AlO_x fillers nano-particulates. Similar results have been observed in other studies of fiber composites with a different aspect ratio of fibers [43].

However, there is a small difference between Young's modulus of nanocomposite (black broken line) and the lower bound of the HS model. This difference increases as the volume fraction of filler increases. The HS model assumes no interaction between filler and matrix, but a real composite always has some degrees of interfacial interaction, which is either physical or chemical. In the case of this study, the contribution of chemical interaction to Young's modulus could be weak because chemical bonds are formed only between liquid-like uncross-linked SU-8 regions (blue region in Fig. 5) and a-AlO_x fillers as in the case for ZnO-infiltrated SU-8 [20]. The chemical bonds that are connected to the soft liquid-like regions should not contribute to Young's modulus much. Thus, the physical interaction between the a-AlO_x filler and SU-8 matrix produces the difference between the experimental data and the HS lower bound primarily. For VPI, the volume fraction of the filler can also be interpreted as the size of the filler because the filler grows as the infiltration cycle (or the volume fraction of the filler) increases. Based on TEM analysis, the size of filler for 12–16 cycles is around 2–3 nm, which appears to be larger than the width of the free volume channel of SU-8 (~0.4 nm in width and a few nm in length based on MD simulation data, **See also Supplementary Information**). This means that the physical interaction between a-AlO_x particulate and SU-8 matrix could increase due to the continuous free volume occupation as the VPI cycle increases.

To test the effect of filler size, MD simulation was also performed with a fullerene filler, which mimics an a-AlO_x particulate

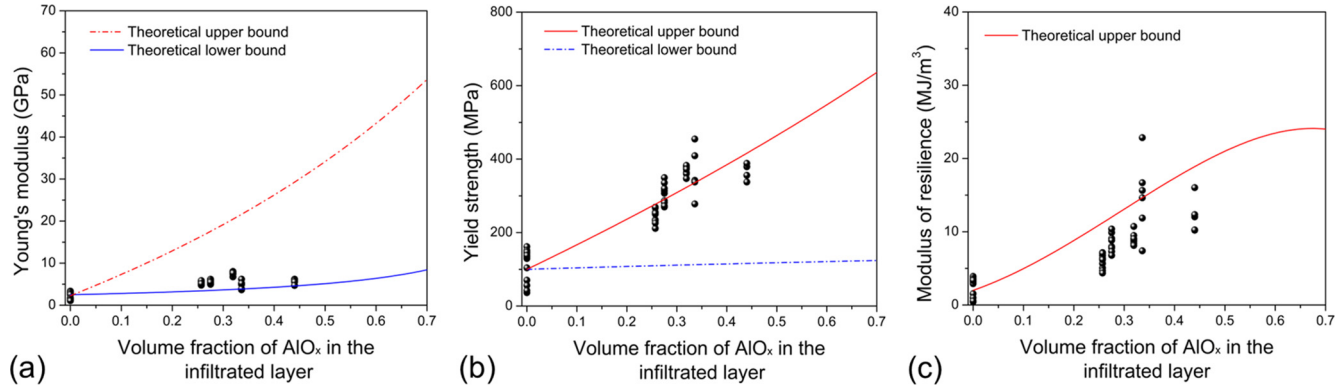

Fig. 10. (a) Comparison of experimental Young's modulus with the upper and lower bounds of the HS model. (b) Comparison of experimental yield strength with the upper and lower bounds of the HS model. (c) Comparison of experimental modulus of resilience with the upper and lower bounds of the HS model.

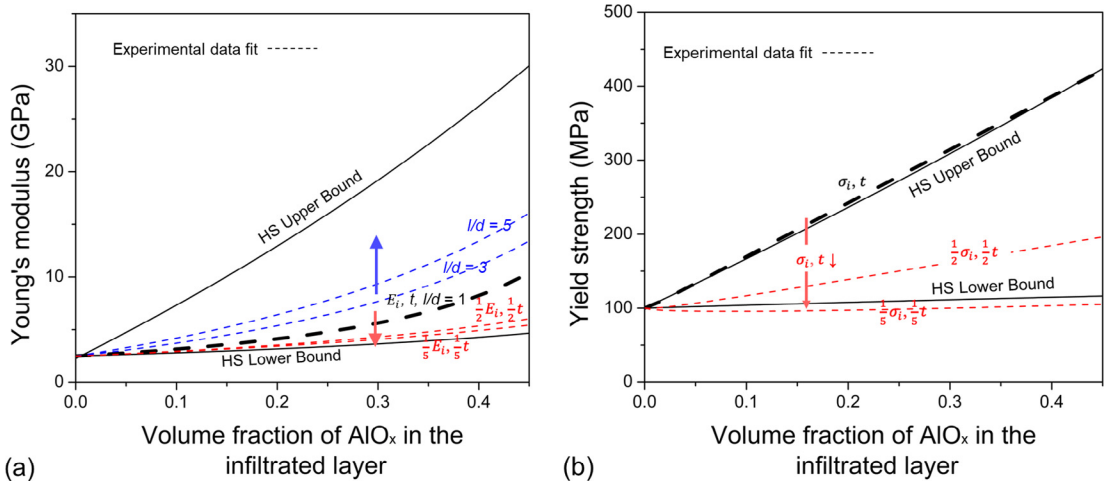

Fig. 11. (a) The influence of the aspect ratio of fillers and the interphase properties (E_i and t) on Young's modulus of SU-8 nanopillar composites as a function of volume fraction of AlO_x. (b) The influence of the aspect ratio of fillers and the interphase properties (σ_i and t) on Young's modulus of SU-8 nanopillar composites as a function of volume fraction of AlO_x.

and allows us to reduce the computational cost due to the small number of atoms of fullerene (**See also Method Section**). The MD simulation results support the hypothesis on the stronger effect of the larger filler size on Young's modulus. The simulated stress–strain data show that a larger filler enhances Young's modulus more effectively than a smaller filler (Fig. 12**(a) and 12(c)**). In MD simulation, before mechanical testing, the energy minimization process moves most small fullerenes into free volume channels because this reduces the total potential energy by minimizing the matrix distortion. Then, at high-volume fractions, the agglomeration of small fullerene molecules in the free volume channels is unavoidable and reduces the load transfer capability significantly due to the weak interaction between fullerenes and the incomplete contact between fullerene agglomerate and matrix (**See also Supplementary Information**). If a filler becomes larger than the free volume, however, all these large fillers are not squeezed into the narrow free volume region. Instead, they will try to stay separately in the matrix. As a result, this uniform distribution of large fillers enables the large contact area and the effective physical interaction between filler and matrix. This is the reason for the higher Young's modulus at the high volume fraction of large fullerenes in MD simulation results and for the higher Young's modulus than the HS lower bound (Fig. 11(a)).

In the mHT model, it is possible to control the degree of interfacial interaction by adjusting the interphase Young's modulus (E_i) and the interphase thickness (t). E_i and t were decreased with the same ratio and confirmed that Young's modulus of composite approaches toward the HS lower bound (Fig. 11**(a)**). In sum, the low Young's modulus of nanocomposite results primarily from the low aspect ratio of nanoscale filler, but Young's modulus is slightly higher than the HS model within the experimental range of volume fraction of a-AlO_x because of the physical interaction at the interface between a-AlO_x filler and SU-8 matrix at the higher infiltration cycle.

4.2. High yield strength

The analysis shows that the yield strength of the nanocomposites is close to the upper bound of the HS model. This is quite surprising because it is usually difficult to get the HS upper bound of mechanical properties with particulate-type fillers. The upper bound of mechanical properties could be obtained from the isostrain model, where a long fiber (or layer) is vertically aligned along the loading direction. Particulate composites usually produce yield strength between lower and upper bounds. Therefore, additional microstructural features, which cannot be found in conventional polymer nanocomposites, are required to bring the yield strength up to the upper bound of the HS model.

First, the effect of interphase on yield strength phenomenologically from the mNN model needs to be evaluated by controlling

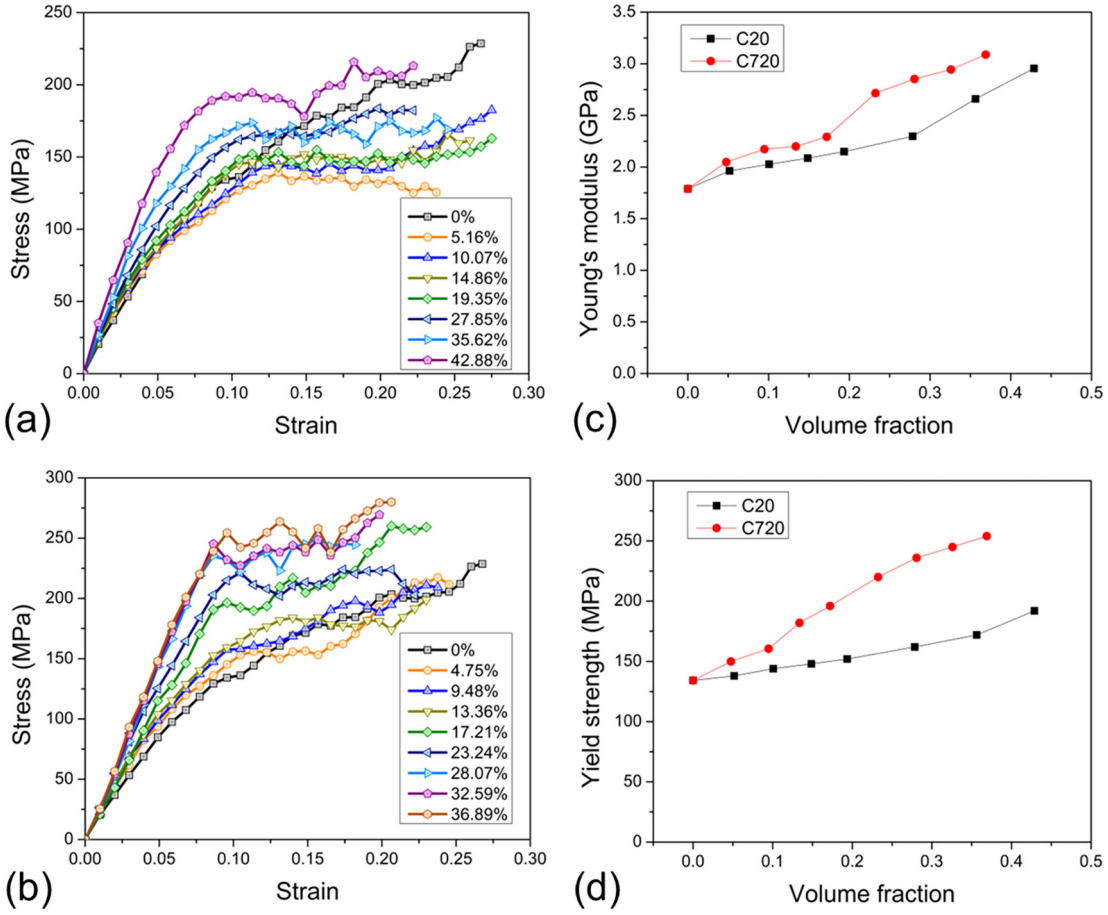

Fig. 12. MD simulation of SU-8 composite uniaxial compression test under 10^8 s^{-1} strain rate. MD simulated stress–strain curves of SU-8 composite with different volume fraction of (a) C20 and (b) C720 fullerene. Comparison of filler size influence on the (c) Young's modulus and (d) yield strength.

the degree of interfacial interaction by adjusting the strength of interphase (σ_i) (Fig. 11**(b)**). One interesting observation is that the effect of interphase on yield strength seems to be much stronger than that of Young's modulus. The interphase yield strength is reduced with the same scale (1/2 and 1/5), which was used to see the effect of interphase on Young's modulus (Fig. 11**(a)**). The yield strength of composites decreases significantly from the upper bound to the lower bound of the HS model. In the mHT model, E_i appears in both numerator and denominator in the expression of η_i, so the change in E_i makes a relatively weak contribution to Young's modulus of the composite. However, σ_i appears only in the numerator in the expression of a. So, σ_i makes a strong influence on the yield strength of the composite. Due to the growth of filler, the filler-matrix physical interaction increases as the volume fraction of filler increases, leading to a more effective load transfer at a higher volume fraction of filler (equivalently, the large size of filler). This is all enabled by the characteristics of VPI that grows nanoscale a-AlO_x particulate fillers in the SU-8 matrix, particularly throughout its free volume.

MD simulations were performed to investigate the effect of filler size on yield strength (Fig. 12**(d)**). A larger fullerene improves yield strength more effectively. Similarly with Young's modulus, a large filler size enables more physical interaction between filler and matrix, which leads to an effective increase in yield strength with the volume fraction of filler. Interestingly, the MD results show that the filler size affects yield strength more than Young's modulus (All other MD data are also available in **Supplementary Information**). The largest (C720) fillers show a 7.5 % higher increase in Young's modulus than the smallest (C20) fillers (Fig. 12**(c)**), but a 46.2 % higher increase in yield strength than the smallest (C20) fillers (Fig. 12**(d)**). The stronger effect of filler size on yield strength must be related to the fundamental difference between plasticity and elasticity of polymer. Under compression, the plastic deformation of polymers usually occurs via the double kink formation or buckling in polymer chains based on the Argon theory, [44] which shows the critical stress of double kink formation as:

$$\tau = \frac{45\mu}{8(1-\nu)} \cdot \left(\frac{r}{z}\right)^6 \tag{11}$$

where μ is the shear modulus, ν is the Poisson's ratio, r is the molecular radius of the polymer chain, and z is the length of the polymer chain. In the case of this stuy, due to the large monomer size and the relatively short chain length, it is difficult to form a double kink. Instead, local buckling of chains can still occur frequently. MD simulations revealed that the two sp^2-sp^3 bonds of benzene ring can be easily rotated, leading to local buckling and re-configuration of chain structures under a stress (**See** Fig. 13 **and Supplementary Movie**). Double-kink formation is basically the combination of two buckling events. Thus, the critical stress of single buckling event could be around the half of Eq. (11), and the similar physical interpretation can be applied to a composite.

Based on Eq. (11), this double kink formation or buckling is directly related to the shear modulus of the polymer matrix, which must be scaled by Young's modulus of the polymer matrix. This part cannot explain the faster increase in yield strength because Young's modulus of polymer matrix itself does not change with compositization due to no chemical mixing between matrix and

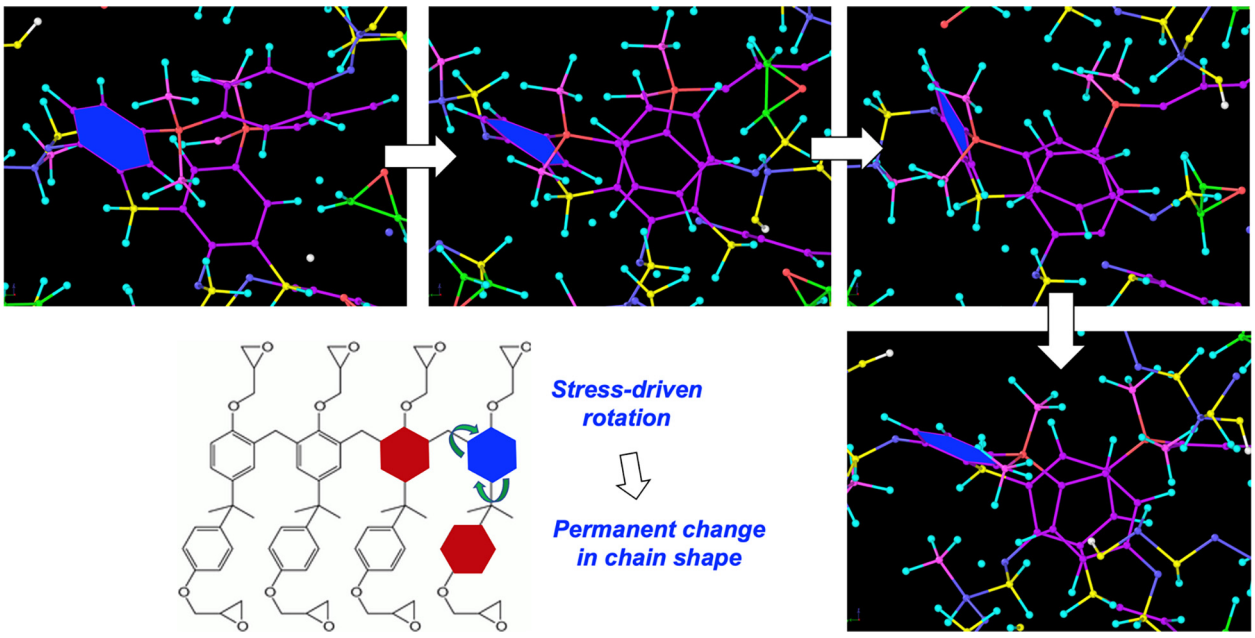

Fig. 13. MD simulation snapshots of the plasticity process in SU-8 matrix. Rotation of benzene ring (blue-colored) along sp2-sp3 bonds allows the local buckling and significant re-configuration of chain structure, leading to the permanent motion (plasticity) of SU-8 chain. Two un-colored benzene rings in snapshots correspond to two red benzene rings in the schematic diagram. The corresponding Supplementary video shows the sudden buckling event due to the rotation of blue benzene ring. (For interpretation of the references to colour in this figure legend, the reader is referred to the web version of this article.)

filler. The presence of a-AlO_x nano-particulates also does not affect the molecular radius (r) of the polymer chain. However, a-AlO_x nano-particulates could effectively reduce the length of the polymer chain because they can serve as an additional anchor in the middle of the polymer chain. The critical stress of buckling is inversely proportional to z^6, and the power of 6 means that the length reduction of polymer chain segments could increase the yield strength of composites significantly. Anchoring effect of a large filler must be more effective than that of small filler because a large filler is more mechanically stable compared to a small filler which moves easily around in a free volume channel. Although the plasticity of SU-8 is related to local buckling event, its elasticity is the volumetric response of atomic bonds and the collective (recoverable) motion of polymer chains under thermodynamic driving force. In this case, the size of the filler is a weak factor, but the volume fraction of the matrix and filler determines Young's modulus of composites more dominantly. For this reason, the yield strength could be more affected by the size of filler (Figs. 7 and 12).

The anchoring effect could be more effective when the particulate size is larger, but the particulate size itself is not enough to explain the high value of σ_i near the upper bound of the HS model because the yield strength of most particulate polymer composites is almost always in between the lower and upper bound of the HS model. [14] Thus, there must be another microstructural feature that can enhance the anchoring mechanism effectively and that cannot be easily seen in conventional solution-based nanocomposites. The STEM EDXS mapping analysis (Fig. 4**(c)**) shows that many fillers are connected by thin a-AlO_x links. These interconnecting links are believed to be formed through the channel among free volume spaces (indicated by the green arrow in Fig. 5). These a-AlO_x links could impact the yield strength significantly because they can immobilize the larger volume of SU-8 matrix. This mechanical locking reduces the length (z in **Eq. (11)**) of the single polymer chain more effectively. This picture is also consistent with the VPI mechanism during which after the initial infiltration cycle, the following infiltration cycles proceed through the interaction of infiltrating precursors (e.g., TMA) with the inorganic inclusion, especially its hydroxyl group, created in the previous infiltration cycle through, thus creating a network of inorganic inclusions penetrating the polymer molecular matrix. [20] In addition, as discussed in the previous section, the distortion of matrix is expected to occur due to filler size being larger than the free volume size. The distorted part of matrix could be denser due to compressive residual stress, which could make the motion of polymer chains more difficult. At a higher volume fraction of large filler, the compressive residual stress could not be negligible everywhere in the SU-8 matrix and could produce the additional resistance to the buckling event because the motion of polymer chains is more restricted by other neighbor chains.

The interphase strength (σ_i) in the mNN model is, in fact, the fitting term that includes all additional strengthening effect other than the effects of particulates. Because the additional effect of interconnecting links and the distorted matrix is included into the interphase strength term and significantly improves the yield strength of nanocomposites, the power value of the volume fraction of the interphase strength (0.2718) is higher than that of the interphase Young's modulus (0.1218) in their power laws. As the volume fraction increases, more interconnecting links will grow, and the matrix distortion will be more significant. Then, the yield strength is more strongly affected by the filler volume fraction than Young's modulus. Overall, the results lead to a notion that the effects of filler size, which are related to the filler-matrix interaction, and thin interconnecting links between nano-particulates and the matrix distortion could result in a significant increase in yield strength, even enabling the yield strength to be nearly close to the upper bound of HS model. Note that, a-AlO_x interconnecting links and the matrix distortion can be only obtained by the VPI method because fillers grow in a free volume channel. These unique features cannot be obtained by conventional solution-based compositization methods, which form a polymer matrix after the insertion of fillers.

4.3. The weak effect of strain rate on the modulus of resilience

Experimental data of modulus of resilience (Fig. 7**(g)-6(i)**) exhibit a relatively weak dependence on strain rate (Fig. 7**(g)-6(i)**). In other words, the nanocomposites can keep a high modulus of resilience regardless of strain rate, and this is beneficial for a high strain rate application, such as artificial muscle or impact protector. The weak effect of strain rate on modulus of resilience results from the stronger effect of strain rate on Young's modulus (E) than that on yield strength (σ_y) according to the experimental data (Fig. 7**(a)-6(f)**). The faster increase in E than σ_y makes $\sigma_y^2/(2E)$ relatively constant.

The strain rate dependence of Young's modulus of polymeric materials is strongly related to viscoelasticity. As a demonstration, the cyclic test with the nominal force amplitude of 0.005 mN and the strain rate of 50 s^{-1} obtained $tan\delta = 1.71$, which implies that the SU-8 matrix is strongly viscoelastic at high strain rate (**See Supplementary Information**). Viscoelasticity of polymeric materials is usually affected by the degree of cross-linking. [45–47] To understand the effect of cross-linking on mechanical properties of polymer nanocomposites, MD simulations were performed with the systematic control of the degree of cross-linking systematically by changing the percentage of cross-linked points from the initial SU-8 chain structure (**See Method Section**). The MD simulation results show that both yield strength and Young's modulus increase as the percentage of cross-linked points increases, but they show the different strain rate dependence (Fig. 14). Particularly at a low percentage of cross-linked points (<50 %), Young's modulus shows the strong strain rate dependence (Fig. 14**(c)**), but yield strength is relatively insensitive to the strain rate (Fig. 14**(d)**). The previous study confirmed that a SU-8 matrix includes non-cross-linked regions (**blue region in** Fig. 5), which could promote the nucleation of nano-particulates. [20] Also, several studies showed that the full cross-linking in SU-8 polymer can be achieved by the high temperature (~240 °C) hard baking or the high exposure dose of electron beam during electron-beam lithography. [48] Note that SU-8 nanopillars were baked only around 90 °C, which is significantly lower than the baking temperature of the full cross-linking condition. The low baking temperature indicates that SU-8 nanopillars in this study could have the relatively low degree of cross-linking, which leads to the higher strain rate dependence of Young's modulus as shown in experimental and MD data (Fig. 7**(a)-6(f)**).

The effect of strain rate on yield strength and Young's modulus can be explained by their fundamental difference in deformation mechanism. If the degree of cross-linking is low, the average length of un-cross-linked chains is longer. Because buckling could occur easily in a longer chain, the Argon theory could be the appropriate model to explain the yield strength of polymer with a low degree of cross-linking. Based on the Argon theory, the yield strength is determined by the critical stress of the double-kink formation or buckling at the structurally weakest spot. In this case, the value of stress at the weakest spot is more important than the rate of stress increase (or strain increase). Regardless of strain rate, once the stress level reaches the critical stress of buckling, plastic deformation could immediately occur. However, the elastic deformation of polymers is mostly the volumetric response because the average

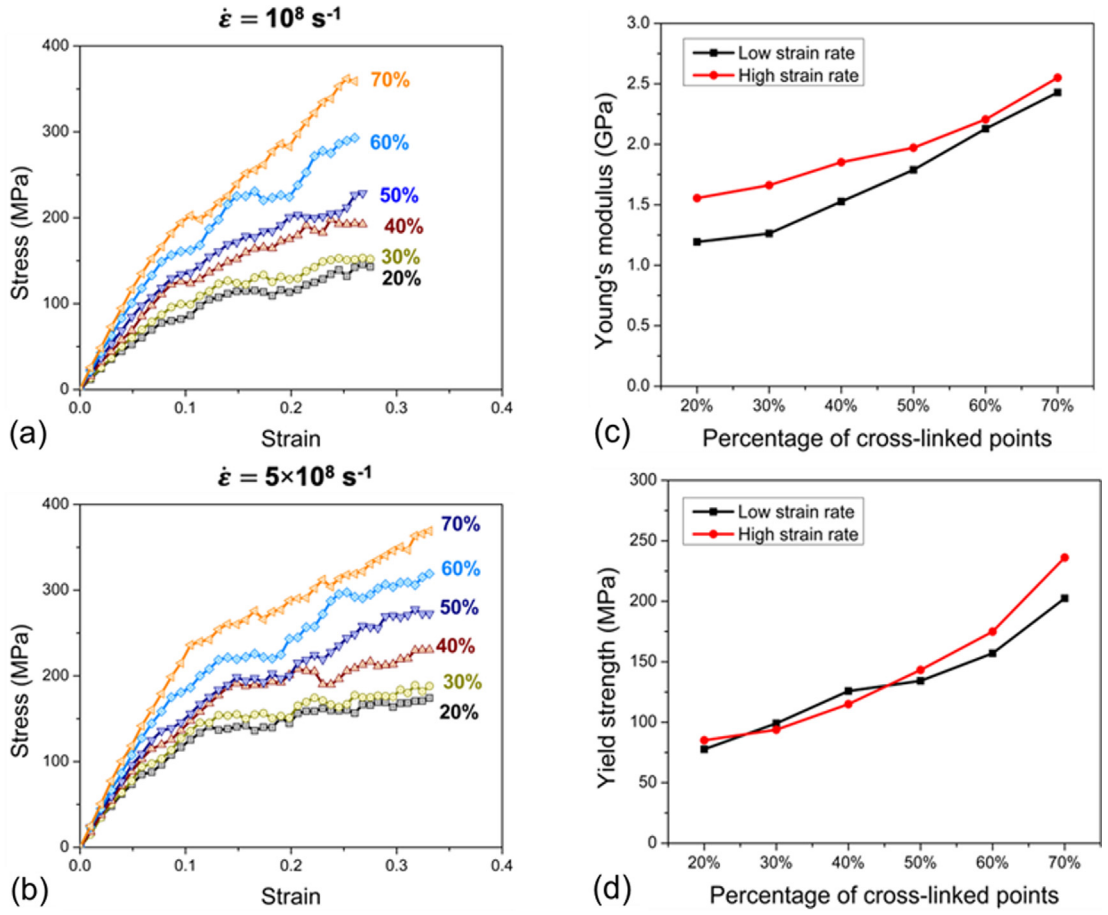

Fig. 14. MD simulation results of uniaxial compression test on pure SU-8. MD simulation stress–strain curves with different cross-linking degrees under the strain rate of (a) 10^8 s^{-1} and (b) $5x10^8$ s^{-1}; (c) Young's modulus and (d) yield strength as a function of percentage of cross-linked points under different strain rate.

motion of polymer chains under the thermodynamic force (entropy change) controls the elastic deformation of polymers. It always takes some time for polymer chains to re-configure their arrangement via thermal vibration under a given stress. Thus, elastic deformation is strongly strain-rate-dependent.

If the degree of cross-linking is high, however, Young's modulus could show a weaker dependence on strain rate because Young's modulus of tightly interconnected polymer structure is controlled by the atomic bonding more than the thermodynamic force. As an extreme case, ceramics or metals exhibit a much weaker strain rate effect on Young's modulus because Young's modulus is controlled completely by atomic bonding, whose elastic response is almost not affected by the strain rate. MD data also show that at a high degree of cross-linking, the yield strength begins to be strain-rate-dependent. Here, we think that the Argon theory does not work anymore because too high stress could be required to cause buckling in a short polymer chain. Then, the yield strength could be not determined by the local deformation but by the collective plastic deformation of tightly interconnected polymer structure. It could take some time to re-arrange the group of tightly connected polymer chains to produce the plastic flow. Therefore, the effect of strain rate on Young's modulus and yield strength can be opposite based on the degree of cross-linking.

Note that MD simulation results are not the same with experimental data. This is most likely because the SU-8 structure of MD simulations may not be identical to the structure of the real SU-8. Also, the strain rate of MD simulations is too high (the order of $10^8 s^{-1}$). It is extremely difficult for MD simulation to mimic the experimental conditions. However, the simulation results qualitatively agree with the experimental observation in that the strain rate effect on Young's modulus is stronger than that on yield strength, providing an important physical insight into understanding of experimental results in terms of the degree of cross-linking.

5. Conclusion

In this study, AlO_x/SU-8 core–shell nanocomposite nanopillars were synthesized via VPI method and confirmed that the nanocomposites exhibit an unusual combination of low Young's modulus and high yield strength. The relationship between the unique composite microstructure and the ultrahigh modulus of resilience of the nanocomposites was investigated by performing nanoindentation, transmission electron microscopy, analytical modeling, and MD simulations. The major findings are shown as follows:

- TEM analysis revealed that the nanopillar composites have a core–shell structure with a ~50 nm thick infiltrated outer layer and a pure SU-8 core with 200 nm in diameter, and the a-AlO_x nano-particulates are dispersed evenly at nanoscale.
- At 12 infiltration cycles, the AlO_x/SU-8 nanocomposites exhibit the metal-like high yield strength (371.13 ± 10.58 MPa) but the polymer-like low Young's modulus (7.66 ± 0.35 GPa), leading to the exceptionally high modulus of resilience (9.02 ± 0.67 MJ/m^3) and specific modulus of resilience (5.21 ± 0.38 kJ/kg). Analytical composite models confirm that the modulus of resilience of the nanocomposites is close to the maximum possible value that can be achieved under the given synthesis conditions.
- The low Young's modulus of nanocomposites could result from the low aspect ratio of a-AlO_x nanoparticulate. The high yield strength could result from the physical interaction between particulate and matrix due to the particulate size larger than the free volume size. Ultra-thin a-AlO_x interconnecting links between nano-particulates enhance anchoring effect, which leads to yield strength close to its theoretical upper bound.
- Uniform distribution of a-AlO_x nanoparticulates with ultrathin interconnecting links cannot be achieved by conventional solution-based compositization methods.
- A stronger dependence of Young's modulus on strain rate than that of yield strength leads to the modulus of resilience value relatively insensitive to the strain rate, which could be due to the low degree of crosslinking in SU-8 polymer matrix.

The results of this work can be useful to improve the sensitivity of MEMS mass sensors. The sensitivity of a MEMS cantilever mass sensor is closely related to the modulus of resilience. The higher the modulus of resilience of cantilever, the high the sensitivity is. If VPI is applied to the existing sensor, its sensitivity can be improved significantly. [11] In addition, VPI can be used simply to strengthen the surface of SU-8 MEMS components. Because VPI does not impact the volume much, the surface of the entire SU-8 MEMS structures could be strengthened through VPI process. This will improve the surface hardness or the wear resistance of the SU-8 MEMS components.

Funding

This work was supported by the National Science Foundation [CMMI-1934829].

Data availability

Data will be made available on request.

Declaration of Competing Interest

The authors declare the following financial interests/personal relationships which may be considered as potential competing interests: Zhongyuan Li reports financial support was provided by National Science Foundation. Seok-Woo Lee reports financial support was provided by National Science Foundation. Ying Li reports financial support was provided by National Science Foundation. Jinlong He reports financial support was provided by National Science Foundation.

Acknowledgment

Z.L., J.H., Y.L., and S.-W.L. gratefully acknowledge financial support from the National Science Foundation (CMMI-1934829). This research used the Materials Synthesis and Characterization, and Electron Microscopy Facilities of the Center for Functional Nanomaterials (CFN), which is a U.S. Department of Energy Office of Science User Facility, at Brookhaven National Laboratory under Contract No. DE-SC0012704.

Appendix A. Supplementary data

Supplementary data to this article can be found online at https://doi.org/10.1016/j.matdes.2023.111770.

References

[1] K. Bluglass, B. Monroe, D. Oliviere, Resilience and Its Narratives. Resilience in palliative care: Achievement in adversity, in: B. Monroe, D. Oliviere (eds.), 2007, pp. 9–28.
[2] J. Zhou, X. Deng, Y. Yan, X. Chen, Y. Liu, Superelasticity and Reversible Energy Absorption of Polyurethane Cellular Structures with Sand Filler, Compos. Struct. 131 (2015) 966–974.
[3] D.M. Costescu, A. Hadăr, Ş.D. Pastramă, DESIGN OF AN ELEMENT USED TO ABSORB THE IMPACT ENERGY FOR A RAILWAY TRANSPORT VEHICLE, 2019, vol. 11.

[4] C. Hong, D. Tang, Q. Quan, Z. Cao, Z. Deng, A Combined Series-Elastic Actuator & Parallel-Elastic Leg No-Latch Bio-Inspired Jumping Robot, Mech Mach Theory 149 (2020) 103814.
[5] J. Lo, B. Parslew, An Energetic Analysis of Rhomboidal Linkage Robots for Hopping Lunar Exploration, in: 2021 Second International Symposium on Instrumentation, Control, Artificial Intelligence, and Robotics (ICA-SYMP); 2021, pp. 1–5.
[6] A. Pal, D. Goswami, R.v. Martinez, Elastic Energy Storage Enables Rapid and Programmable Actuation in Soft Machines, Adv. Funct. Mater. 30 (2020) 1906603.
[7] R.D. Rodriguez, S. Shchadenko, G. Murastov, A. Lipovka, M. Fatkullin, I. Petrov, T.-H. Tran, A. Khalelov, M. Saqib, N.E. Villa, V. Bogoslovskiy, Y. Wang, C.-G. Hu, A. Zinovyev, W. Sheng, J.-J. Chen, I. Amin, E. Sheremet, Ultra-Robust Flexible Electronics by Laser-Driven Polymer-Nanomaterials Integration, Adv. Funct. Mater. 31 (2021) 2008818.
[8] Z. Ji, X. Zhang, C. Yan, X. Jia, Y. Xia, X. Wang, F. Zhou, 3D Printing of Photocuring Elastomers with Excellent Mechanical Strength and Resilience, Macromol. Rapid Commun. 40 (2019) 1800873.
[9] S.A. Fedorov, N.J. Engelsen, A.H. Ghadimi, M.J. Bereyhi, R. Schilling, D.J. Wilson, T.J. Kippenberg, Generalized Dissipation Dilution in Strained Mechanical Resonators, Phys. Rev. B 99 (2019) 54107.
[10] Q.P. Unterreithmeier, T. Faust, J.P. Kotthaus, Damping of Nanomechanical Resonators, Phys. Rev. Lett. 105 (2010) 27205.
[11] L. Sang, M. Liao, X. Yang, H. Sun, J. Zhang, M. Sumiya, B. Shen, Strain-Enhanced High Q-Factor GaN Micro-Electromechanical Resonator, Sci. Technol. Adv. Mater. 21 (2020) 515–523.
[12] M.F. Ashby, Chapter 4 - Material Property Charts, in: M.F. Ashby (Ed.), Materials Selection in Mechanical Design, Fourth Edition., Butterworth-Heinemann, Oxford, 2011, pp. 57–96.
[13] Z. Hashin, S. Shtrikman, A Variational Approach to the Theory of the Elastic Behaviour of Multiphase Materials, J. Mech. Phys. Solids 11 (1963) 127–140.
[14] P. Ponte Castañeda, G. DeBotton, M.E. Fisher, On the Homogenized Yield Strength of Two-Phase Composites, in: Proceedings of the Royal Society of London. Series A: Mathematical and Physical Sciences, 1992, 438, pp. 419–431.
[15] M.A. Ashraf, W. Peng, Y. Zare, K.Y. Rhee, Effects of Size and Aggregation/Agglomeration of Nanoparticles on the Interfacial/Interphase Properties and Tensile Strength of Polymer Nanocomposites, Nanoscale Res Lett 13 (2018) 214.
[16] M.A. Kashfipour, N. Mehra, J. Zhu, A Review on the Role of Interface in Mechanical, Thermal, and Electrical Properties of Polymer Composites, Adv Compos Hybrid Mater 1 (2018) 415–439.
[17] P.K. Balguri, D.G.H. Samuel, U. Thumu, A Review on Mechanical Properties of Epoxy Nanocomposites, Mater Today Proc 44 (2021) 346–355.
[18] A. Siot, C. Longuet, R. Léger, B. Otazaghine, P. Ienny, A.-S. Caro-Bretelle, N. Azéma, Correlation between Process and Silica Dispersion/Distribution into Composite: Impact on Mechanical Properties and Weibull Statistical Analysis, Polym Test 70 (2018) 92–101.
[19] S. Mondal, P. Das, S. Ganguly, R. Ravindren, S. Remanan, P. Bhawal, T.K. Das, N. C. Das, Thermal-Air Ageing Treatment on Mechanical, Electrical, and Electromagnetic Interference Shielding Properties of Lightweight Carbon Nanotube Based Polymer Nanocomposites, Compos Part A Appl Sci Manuf 107 (2018) 447–460.
[20] X. Ye, J. Kestell, K. Kisslinger, M. Liu, R.B. Grubbs, J.A. Boscoboinik, C.-Y. Nam, Effects of Residual Solvent Molecules Facilitating the Infiltration Synthesis of ZnO in a Nonreactive Polymer, Chem. Mater. 29 (2017) 4535–4545.
[21] J. Pilz, A.M. Coclite, M.D. Losego, Vapor Phase Infiltration of Zinc Oxide into Thin Films of Cis-Polyisoprene Rubber, Mater Adv 1 (6) (2020) 1695–1704.
[22] B.C. Jean, Y. Ren, E.K. McGuinness, R.P. Lively, M.D. Losego, Effects of Trimethylaluminum Vapor Pressure and Exposure Time on Inorganic Loading in Vapor Phase Infiltrated PIM-1 Polymer Membranes, Mater Chem Phys 290 (2022) 126577.
[23] A. Subramanian, N. Tiwale, C.-Y. Nam, Review of Recent Advances in Applications of Vapor-Phase Material Infiltration Based on Atomic Layer Deposition, JOM 71 (2019) 185–196.
[24] K.J. Dusoe, X. Ye, K. Kisslinger, A. Stein, S.-W. Lee, C.-Y. Nam, Ultrahigh Elastic Strain Energy Storage in Metal-Oxide-Infiltrated Patterned Hybrid Polymer Nanocomposites, Nano Lett. 17 (2017) 7416–7423.
[25] Y. Zare, Development of Halpin-Tsai Model for Polymer Nanocomposites Assuming Interphase Properties and Nanofiller Size, Polym. Test. 51 (2016) 69–73.
[26] Y. Zare, Development of Nicolais-Narkis Model for Yield Strength of Polymer Nanocomposites Reinforced with Spherical Nanoparticles, Int. J. Adhes. Adhes. 70 (2016) 191–195.
[27] A. Subramanian, G. Doerk, K. Kisslinger, D.H. Yi, R.B. Grubbs, C.-Y. Nam, Three-Dimensional Electroactive ZnO Nanomesh Directly Derived from Hierarchically Self-Assembled Block Copolymer Thin Films, Nanoscale 11 (2019) 9533–9546.
[28] S. Plimpton, Fast Parallel Algorithms for Short-Range Molecular Dynamics, J. Comput. Phys. 117 (1995) 1–19.
[29] H. Heinz, T.-J. Lin, R. Kishore Mishra, F.S. Emami, Thermodynamically Consistent Force Fields for the Assembly of Inorganic, Organic, and Biological Nanostructures: The INTERFACE Force Field, Langmuir 29 (2013) 1754–1765.
[30] H. Sun, S.J. Mumby, J.R. Maple, A.T. Hagler, An Ab-Initio Cff93 All-Atom Force-Field for Polycarbonates, J Am Chem Soc 116 (1994) 2978–2987.
[31] H. Sun, Ab-Initio Calculations and Force-Field Development for Computer-Simulation of Polysilanes, Macromolecules 28 (1995) 701–712.
[32] H. Sun, COMPASS: An Ab Initio Force-Field Optimized for Condensed-Phase Applications Overview with Details on Alkane and Benzene Compounds, J. Phys. Chem. B 102 (1998) 7338–7364.
[33] L.J. Abbott, K.E. Hart, C.M. Colina, Polymatic: A Generalized Simulated Polymerization Algorithm for Amorphous Polymers, Theor Chem Acc 132 (2013) 1334.
[34] Z. Zhang, Y. Wang, P. Liu, T. Chen, G. Hou, L. Xu, X. Wang, Z. Hu, J. Liu, L. Zhang, Quantitatively Predicting the Mechanical Behavior of Elastomers via Fully Atomistic Molecular Dynamics Simulation, Polymer (Guildf) 223 (2021) 123704.
[35] S. Kumar Singh, A. Kumar, A. Jain, Improving Tensile and Flexural Properties of SiO2-Epoxy Polymer Nanocomposite, Mater Today Proc 5 (2018) 6339–6344.
[36] K. Kumar, P.K. Ghosh, A. Kumar, O. Singh, Enhanced Thermomechanical Properties of ZrO2 Particle Reinforced Epoxy Nanocomposite, J Mater Eng Perform 30 (2021) 145–153.
[37] C. Xiao, Y. Tan, X. Yang, T. Xu, L. Wang, Z. Qi, Mechanical Properties and Strengthening Mechanism of Epoxy Resin Reinforced with Nano-SiO2 Particles and Multi-Walled Carbon Nanotubes, Chem Phys Lett 695 (2018) 34–43.
[38] F.G. Torres, S.N. Nazhat, S.H. Sheikh Md Fadzullah, V. Maquet, A.R. Boccaccini, Mechanical Properties and Bioactivity of Porous PLGA/TiO2 Nanoparticle-Filled Composites for Tissue Engineering Scaffolds, Compos. Sci. Technol. 67 (2007) 1139–1147.
[39] J.C.H. Affdl, J.L. Kardos, The Halpin-Tsai Equations: A Review, Polym Eng Sci 16 (1976) 344–352.
[40] M.K. Tripp, C. Stampfer, D.C. Miller, T. Helbling, C.F. Herrmann, C. Hierold, K. Gall, S.M. George, V.M. Bright, The Mechanical Properties of Atomic Layer Deposited Alumina for Use in Micro- and Nano-Electromechanical Systems, Sens. Actuators, A 130–131 (2006) 419–429.
[41] G. Simmons, Single Crystal Elastic Constants and Calculated Aggregate Properties: A Handbook, 2nd ed., M.I.T. Press Cambridge, MA, 1971.
[42] C. Luo, T.W. Schneider, R.C. White, J. Currie, M. Paranjape, A Simple Deflection-Testing Method to Determine Poisson s Ratio for MEMS Applications, J. Micromech. Microeng. 13 (2002) 129–133.
[43] R.L. Foye, An evaluation of various engineering estimates of the transverse properties of unidirectional composites, in: Proceedings of the Tenth National SAMP E Symposiwn-Advanced Fibrous Reinforced composites, 1966, pp. 9-11.
[44] V. Sundararaghavan, A. Kumar, Molecular Dynamics Simulations of Compressive Yielding in Cross-Linked Epoxies in the Context of Argon Theory, Int. J. Plast 47 (2013) 111–125.
[45] J. Shen, X. Lin, J. Liu, X. Li, Effects of Cross-Link Density and Distribution on Static and Dynamic Properties of Chemically Cross-Linked Polymers, Macromolecules 52 (2019) 121–134.
[46] Y. Liu, Z. Tang, J. Chen, J. Xiong, D. Wang, S. Wang, S. Wu, B. Guo, Tuning the Mechanical and Dynamic Properties of Imine Bond Crosslinked Elastomeric Vitrimers by Manipulating the Crosslinking Degree, Polym Chem 11 (2020) 1348–1355.
[47] J. Lou, S. Friedowitz, K. Will, J. Qin, Y. Xia, Predictably Engineering the Viscoelastic Behavior of Dynamic Hydrogels via Correlation with Molecular Parameters, Adv. Mater. 33 (2021) 2104460.
[48] T. Winterstein, M. Staab, C. Nakic, H.-J. Feige, J. Vogel, H.F. Schlaak, SU-8 Electrothermal Actuators: Optimization of Fabrication and Excitation for Long-Term Use, Micromachines (Basel) 5 (2014) 1310–1322.